

# Retinoschisin Deficiency Induces Persistent Aberrant Waves of Activity Affecting Neuroglial Signaling in the Retina

Cyril G. Eleftheriou,<sup>1</sup> Carlo Corona,<sup>1</sup> Shireen Khattak,<sup>2</sup> Nazia M. Alam,<sup>1</sup> Elena Ivanova,<sup>1,2</sup> Paola Bianchimano,<sup>1</sup> Yang Liu,<sup>2</sup> Duo Sun,<sup>2</sup> Rupesh Singh,<sup>3</sup> Julia C. Batoki,<sup>3</sup> Glen T. Prusky,<sup>1</sup> J. Jason McAnany,<sup>4</sup> Neal S. Peachey,<sup>3,5,6</sup> Carmelo Romano,<sup>2</sup> and Botir T. Sagdullaev<sup>1,2</sup>

<sup>1</sup>Burke Neurological Institute, Weill Cornell Medicine, White Plains, New York 10605, <sup>2</sup>Regeneron Pharmaceuticals, Tarrytown, New York 10591, <sup>3</sup>Cole Eye Institute, Cleveland Clinic, Cleveland, Ohio 44195, <sup>4</sup>Department of Ophthalmology, College of Medicine, University of Illinois at Chicago, Chicago, Illinois 60612, <sup>5</sup>Louis Stokes Cleveland VA Medical Center, Cleveland, Ohio 44106, and <sup>6</sup>Department of Ophthalmology, Cleveland Clinic Lerner College of Medicine of Case Western Reserve University, Cleveland, Ohio 44195

Genetic disorders that present during development make treatment strategies particularly challenging because there is a need to disentangle primary pathophysiology from downstream dysfunction caused at key developmental stages. To provide a deeper insight into this question, we studied a mouse model of X-linked juvenile retinoschisis, an early-onset inherited condition caused by mutations in the *Rsl* gene encoding retinoschisin (RS1) and characterized by cystic retinal lesions and early visual deficits. Using an unbiased approach in expressing the fast intracellular calcium indicator GCaMP6f in neuronal, glial, and vascular cells of the retina of RS1-deficient male mice, we found that initial cyst formation is paralleled by the appearance of aberrant spontaneous neuroglial signals as early as postnatal day 15, when eyes normally open. These presented as glutamate-driven wavelets of neuronal activity and sporadic radial bursts of activity by Müller glia, spanning all retinal layers and disrupting light-induced signaling. This study confers a role to RS1 beyond its function as an adhesion molecule, identifies an early onset for dysfunction in the course of disease, establishing a potential window for disease diagnosis and therapeutic intervention.

**Key words:** aberrant activity; neuroglia; optophysiology; retinal waves; retinoschisin

## Significance Statement

Developmental disorders make it difficult to distinguish pathophysiology due to ongoing disease from pathophysiology due to disrupted development. Here, we investigated a mouse model for X-linked retinoschisis, a well defined monogenic degenerative disease caused by mutations in the *Rsl* gene, which codes for the protein retinoschisin. We evaluated the spontaneous activity of explanted retinas lacking retinoschisin at key stages of development using the unbiased approach of ubiquitously expressing GCaMP6f in all retinal neurons, vasculature, and glia. In mice lacking RS1, we found that an array of novel phenotypes, which present around eye opening, are linked to glutamatergic neurotransmission and affect visual processing. These data identify a novel pathophysiology linked to RS1, and define a window where treatments might be best targeted.

Received Oct. 25, 2021; revised July 18, 2022; accepted July 22, 2022.

Author contributions: C.G.E., C.C., S.K., N.M.A., E.I., P.B., Y.L., D.S., R.S., J.C.B., G.T.P., J.J.M., N.S.P., C.R., and B.T.S. designed research; C.G.E., C.C., S.K., N.M.A., E.I., P.B., Y.L., D.S., R.S., J.C.B., G.T.P., and B.T.S. performed research; C.G.E. contributed unpublished reagents/analytic tools; C.G.E., S.K., N.M.A., E.I., G.T.P., N.S.P., and B.T.S. analyzed data; C.G.E., N.S.P., and B.T.S. wrote the paper.

This work was supported by National Institutes of Health Grants [R01-EY-029796 (to N.S.P., J.J.M., and B.T.S.) and R01-EY-026576 to B.T.S.] and by core grants to the Departments of Ophthalmology of the Cleveland Clinic Lerner College of Medicine of Case Western Reserve University (CCLCM of CWRU); Grant P30-EY-025585, and the University of Illinois at Chicago College of Medicine (UIC COM; Grant P30-EY-001792); by unrestricted grants from Research to Prevent Blindness to the Departments of Ophthalmology of CCLCM of CWRU and UIC COM; and by Regeneron Pharmaceuticals. The authors also acknowledge the Structural and Functional Imaging Core at Burke Neurological Institute and NIH S10 shared Instrumentation Grant OD028547-01 for supporting this work. We thank Susan Croll for helpful discussions on biostatistics, and Lampros Panagis for help with setting up imaging of retinoschisin protein and RNA.

S.K., E.I., Y.L., D.S., C.R., and B.T.S. are employees of Regeneron Pharmaceuticals. The authors declare no other competing financial interests.

Correspondence should be addressed to Botir T. Sagdullaev at botir.sagdullaev@regeneron.com.

<https://doi.org/10.1523/JNEUROSCI.2128-21.2022>

Copyright © 2022 the authors

## Introduction

X-linked retinoschisis (XLRS; Online Mendelian Inheritance in Man #312700) is a leading cause of early-onset macular degeneration in males. XLRS is characterized by a splitting of the retinal layers (Molday et al., 2012) with cystic-appearing lesions most apparent in the central macula, but with many patients also developing peripheral pathology (George et al., 1995). Functional diagnostics have uncovered significant losses in visual acuity and contrast sensitivity, as well as amplitude reduction of the electroretinogram (Forsius et al., 1973; Tanino et al., 1985; Peachey et al., 1987; Alexander et al., 2005). XLRS is the result of mutations in the *RS1* gene, which encodes retinoschisin (RS1), an extracellular protein exclusive to the retina (Sauer et al., 1997). However, there still exists several gaps in knowledge, especially at early developmental stages.

RS1 is secreted primarily by photoreceptors in the mature mouse retina (Liu et al., 2019). Whereas RS1 is observed in inner retinal cells during development (Takada et al., 2004; Liu et al., 2019), the functional consequences of this expression is not clear. The protein consists of disulfide bond-stabilized homodimers, which assemble intracellularly (Molday et al., 2012) in octamer pairs displaying a symmetrical cog wheel-like structure (Bush et al., 2016; Tolun et al., 2016). This rugged topography, along with the anatomic features of retinal splitting in the absence of RS1, is consistent with the proposed role for RS1 as a retinal adhesion molecule (Wu et al., 2005). RS1 has also been identified as a binding partner for the  $\alpha 3 \beta 2$  isoform of the Na/K ATPase at the surface of photoreceptors and may also regulate intracellular signaling (Molday et al., 2007; Plössl et al., 2017a,b). Our recent work (Liu et al., 2019) identified that in RS1-deficient mice horizontal cells (HCs) and rod bipolar cells abnormally extended their neurites past the outer plexiform layer (OPL) and into the outer nuclear layer (ONL). These anatomic defects indicated a role for RS1 in controlling glutamate release from photoreceptor terminals, a hypothesis that was further supported by functional studies identifying both presynaptic and postsynaptic abnormalities at the glutamatergic photoreceptor-to-ON bipolar cell (BC) synapse of *Rs1*<sup>-/-</sup> (KO) mice (Ou et al., 2015). In this study, we used calcium imaging optophysiology to further investigate the link between defects at the OPL, vision loss, and retinal cyst formation.

Our results revealed aberrant neuronal signals that we termed “wavelets,” which persisted after eye opening in KO mice and originated in the OFF portion of the inner plexiform layer (IPL). Aberrant activity was also detected in clusters of Müller cell (MC) glia, which exhibited spontaneous and coordinated ripples of calcium fluorescence. These propagated radially in both control and KO mice but were significantly larger and more frequent in KO than in control retinas. Abnormal wavelets and aberrant glial signals were driven by glutamatergic neurotransmission. Using *in vivo* spectral-domain optical coherence tomography (SD-OCT) imaging, we report that retinoschisis is identifiable at postnatal day 13 (P13), but was not observed at P11, in three *Rs1* mutant models, raising the possibility that initial retinal development may proceed normally in the absence of wild-type (WT) RS1. This time course coincided with the period when RS1 protein can first be identified outside of the photoreceptor inner segments.

Our findings provide new insights into the pathophysiology of mutant RS1 by defining a role for neuroglial cells of the retina in RS1 function. We also establish a time window at which the onset of retinal dysfunction coincides with RS1 appearance outside of photoreceptor inner segments. By identifying a novel role for RS1 in retinal development, our results support the hypothesis that RS1 is essential for the maturation of retinal circuitry, beyond its role as an adhesion molecule. Further, our results suggest an intimate relationship between RS1 and normal glutamatergic synapse formation.

## Materials and Methods

### Animals

Experimental animals were treated in compliance with protocols approved by the Institutional Animal Care and Use Committees of Weill Cornell Medicine (WCM), Cleveland Clinic (CC), or Regeneron Pharmaceuticals (RP), and in accordance with the National Institutes of Health (NIH) *Guide for the Care and Use of Laboratory Animals*. For *in vivo* imaging conducted at CC, we examined the following three *Rs1* mutant lines: a KO with inserted lacZ reporter gene (*Rs1*<sup>lacZ</sup>; *Rs*<sup>-/-</sup>); a

C59S point mutant substitution (*Rs1*<sup>C59S/Y</sup>; *Rs1*<sup>C59S/C59S</sup>; hereafter C59S); and an R141C point mutant substitution (*Rs1*<sup>R141C/Y</sup>; *Rs1*<sup>R141C/R141C</sup>; hereafter called R141C; Liu et al., 2019). Controls were an F1 hybrid (F1 hybrid 129S6SvEvTac/C57BL6NTac). For the developmental analysis of *Rs1* expression and RS1 localization conducted at RP, we worked with KO and C57BL/6 mice obtained from The Jackson Laboratory and Taconic. For optophysiology, optokinetic tracking, and immunohistochemistry (IHC) studies conducted at WCM, we crossed KO females with males from our NG2-GCaMP6f line generated by crossing a floxed GCaMP6f line with NG2 Cre transgenic mice (Kovacs-Oller et al., 2020). Control animals were a cross between C57BL/6j females and male NG2 GCaMP6f. Only male offspring who carried the NG2 Cre and floxed GCaMP6f alleles were used for optophysiological experiments.

### RS1 expression

**Tissue collection.** Following killing, a corneal burn at the 12 o'clock position was made in the retina to provide a fiducial landmark. Enucleated eyes were fixed in 4% paraformaldehyde (PFA) for 24 h at 4°C, and a cut was made in the central cornea to allow the fixative to enter the posterior chamber. Following fixation, eyes were washed three times for 15 min in 1× PBS. The anterior chamber (cornea and iris) of each eye was dissected and removed, and a small cut was made near the corneal burn to establish orientation. Posterior eyecups were then incubated overnight at 4°C with 15% and then 30% sucrose solutions. Cryoprotected eyecups were embedded in a cryomold containing a 2:1 solution of Tissue-Tek O.C.T. compound (Sakura Finetek) and 30% sucrose, and flash frozen in 2-methylbutane on dry ice. During embedding, the orientation of the eyecup in the mold was kept consistent, with the posterior pole at the bottom of the mold and the optic nerve facing away from the label. Frozen tissue blocks were stored at −80°C until cryosectioning. Ten-micrometer-thick serial cryosections obtained with a cryostat (model CM3050S, Leica) at the level of the optic nerve were mounted on charged slides (Superfrost Plus Micro Slides; catalog #48311–703, VWR). The tissue block was oriented so that sagittal sections were collected through the nasal–temporal plane. Mounted sections were dried for 1 h at room temperature (RT) and then stored at −80°C until further processing.

**Immunohistochemistry.** To reduce nonspecific binding of the anti-mouse secondary antibody to blood vessels, 100 µg of the primary antibody against RS1 protein (catalog #H00006247-B01P, Abnova) was directly conjugated to Alexa Fluor 647 (hereafter called RS1-AF647) using a site-specific antibody labeling kit (SiteClick Antibody Azido Modification Kit; catalog #S0026, Thermo Fisher Scientific; SiteClick Alexa Fluor 647 sDIBO Alkyne; catalog #S10906, Thermo Fisher Scientific). Following the final wash step in the protein concentrator, the volume was concentrated to 100 µl to achieve an approximate antibody concentration of 1 µg/µl. Sections were emersed in a blocking buffer containing 5% goat serum (catalog #16210–064, Thermo Fisher Scientific), 1% bovine serum albumin (catalog #A4503, Sigma-Aldrich), and 0.5% Triton-X (catalog #93443, Sigma-Aldrich) for 1 h at room temperature. Sections were then incubated overnight at 4°C with the RS1-AF647 antibody in blocking buffer (1:100 dilution). Following incubation, slides were washed three times for 5 min with 1× PBS containing 0.1% Tween-20 (catalog #P9416, Sigma-Aldrich), and two times for 5 min with 1× PBS. Excess PBS was carefully removed, and sections were mounted on no. 1.5 glass coverslips (catalog #106004–340, VWR) with an anti-fade mounting medium and a DAPI counterstain (catalog #P36931, Thermo Fisher Scientific).

**In situ hybridization.** Slides were washed in distilled water, dipped in 100% ethanol, and allowed to dry overnight at room temperature. Sections were then pretreated with H<sub>2</sub>O<sub>2</sub> (catalog #322330, A.C.D.) for 10 min at room temperature, boiled with a steamer in antigen retrieval buffer (10× diluted in distilled H<sub>2</sub>O; catalog #322001, A.C.D.) for 15 min (Oster Steamer; model 5709, IHC World), and treated with Protease Plus (catalog #322330, A.C.D.) for 30 min at room temperature. At this stage, an additional DNase treatment step was included to reduce background signal from the probe binding to chromosomal DNA. A solution of DNase I (50 U/ml in 1× DNase buffer; catalog #AM224, Ambion) was added to the sections and incubated at 40°C for



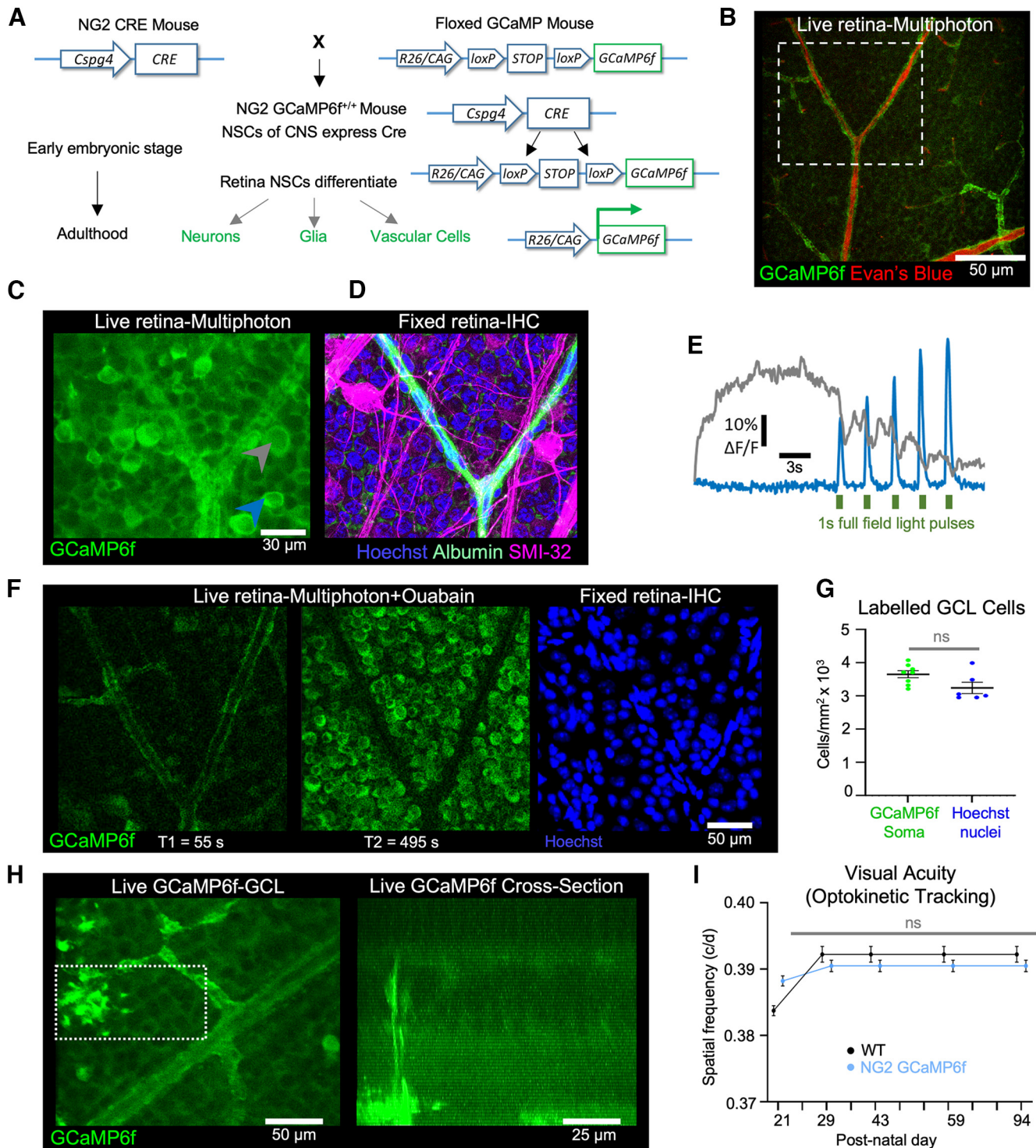


**Figure 1.** Generating NG2 GCaMP6f mice to characterize calcium dynamics in retinal cells. **A**, The NG2 Cre parent (left) expresses Cre recombinase under the Cspg4 promoter, active in all neuroglia cells at early embryonic stages. The floxed GCaMP parent (right) expresses a floxed stop cassette upstream of the GCaMP6f sensor construct on the Gt(ROSA)26Sor locus, downstream of the ubiquitous CAG promoter. **B**, Multiphoton imaging of the calcium dynamics in neurons, vascular cells, and glia via the green channel simultaneous with mapping the local vascular system (injected with Evans blue) for *post hoc* immunohistochemical analyses via the red channel. **C**, Portion of retina in **B** (white box) highlighting several fluorescent retinal ganglion cells and vascular cells. **D**, Retinas in **B** and **C** stained for a subpopulation of neurons ( $\alpha$ RGs, SMI-32; magenta) and nuclei in the GCL (blue). Elongated nuclei of vascular cells indicate the shape of local vasculature. **E**, The 30 s fluorescent traces of cells indicated in **C** with the neuronal traces (gray and blue) showing fast responses to light stimulation (5 × 1 s pulses every 5 s; green). **F**, To evaluate the number of neurons expressing GCaMP6f in our mouse model, we depolarized all cells by superfusing our live preparation with 10  $\mu$ M ouabain. Most neurons were depolarized at 405 s (T2) after the onset of ouabain application. The same portion of retinal tissue was fixed and stained for nuclear DNA (Hoechst; right). **G**, The fraction of ouabain-depolarized cells per square millimeter did not significantly defer from the fraction of Hoechst-stained nuclei in the GCL for six retinas (Mann–Whitney test,  $p = 0.0813$ ). **H**, Localized intracellular calcium increase in Müller cells as seen from the GCL (left), and throughout the retina (right; imaged using live z-stack imaging). **I**, NG2 GCaMP (control) and WT mice had similar visual acuity up to an age of 94 postnatal days (Kruskal–Wallis test with multiple comparisons,  $p > 0.9999$  at each time point). non-significant (ns)  $p > 0.05$ .



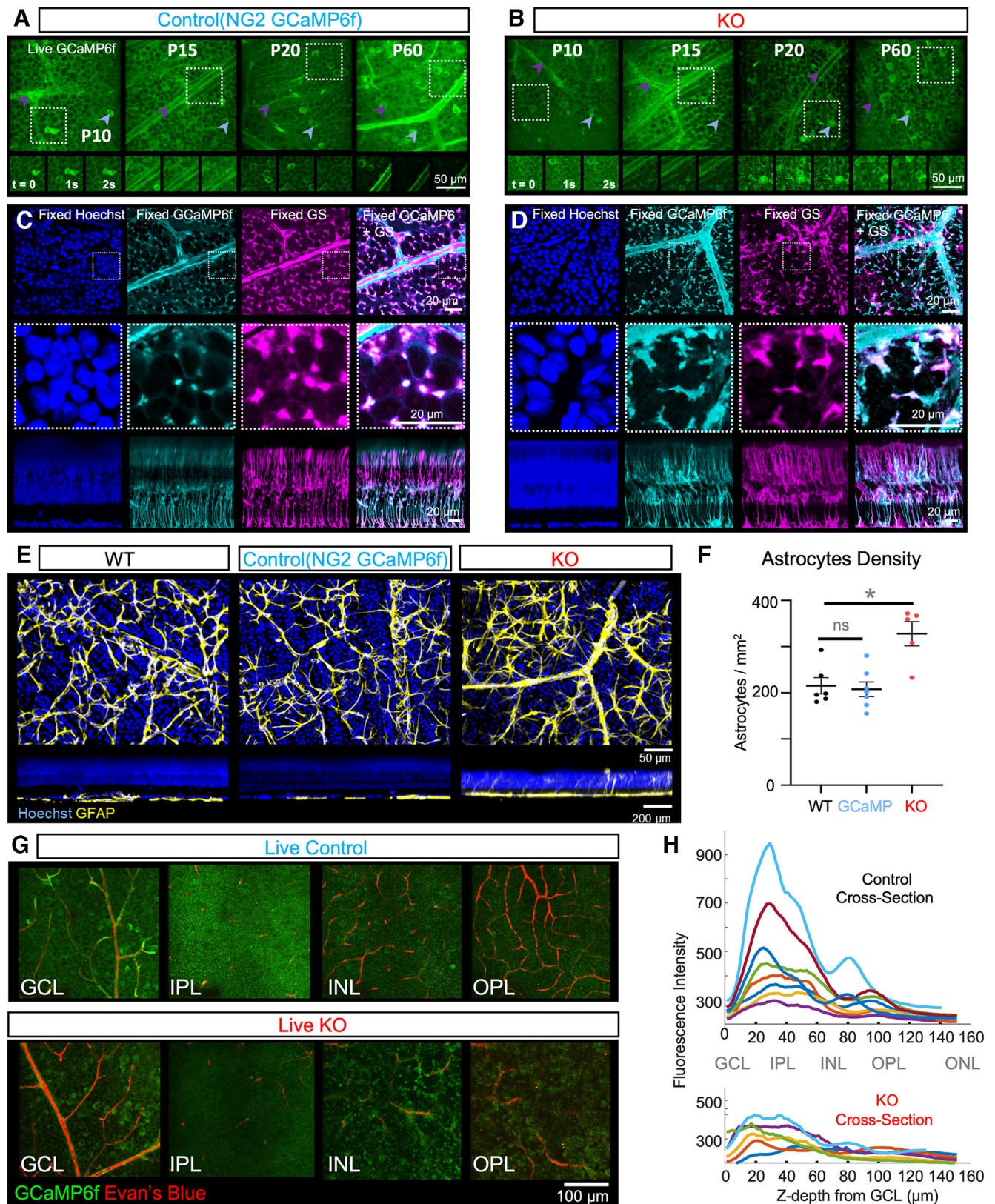


**Figure 2.** Neuro-glio-vascular characterization of control and KO retinas. **A, B**, Dynamic fluorescence is maintained in neurons (blue arrowheads) and vascular cells (purple arrowheads) throughout development and in the adult control (**A**) and KO (**B**) retinas. **C, D**, Fixed tissue in control (**C**) and KO (**D**) retinas stained for nuclei (Hoechst; blue), GS (magenta), and expressing endogenous GCaMP (cyan) showing overlapping expression in the GCL (top, middle) and throughout the retina (bottom), highlighting the colocalized expression of GCaMP in Müller cells. **E**, Micrographs of WT, NG2 GCaMP (control), and control NG2 GCaMP Rs1y/– (KO) retinas stained for GFAP (yellow) and Hoechst (blue), displaying a projected 5  $\mu$ m stack of the GCL (top) and a 3D projected stack of the transverse retina (bottom). **F**, Astrocytic density was significantly higher in NG2 GCaMP RS1y/– (KO) but not in NG2 GCaMP (control) when compared with WT mice retinas (Mann–Whitney test,  $p = 0.0234$  and  $p > 0.9999$ , respectively). **G**, Live control retina (top) displays typical lamination profile, with blood vessels delimiting GCL, INL, and OPL. KO retinas (bottom) display fibrous appearance in non-neuronal layers. **H**, The z profile of GCaMP6f fluorescence from eight control retinas display a bimodal distribution, with peaks in the synaptic



30 min. Sections were washed three times in distilled water and hybridized with an RNAScope probe that recognized mouse *Rs1* mRNA (catalog #456821, A.C.D.). The remainder of the protocol was implemented according to the manufacturer protocol (RNAScope 2.5 HD Detection Reagent RED; catalog #322360, Advanced Cell Diagnostics). Following the final wash step, slides were counterstained with DAPI (1:250 in 1× PBS, 10 min at RT; catalog #564907, BD Pharmingen) and mounted with Prolong Glass anti-fade mounting medium (catalog #P36980, Thermo Fisher Scientific) using no. 1.5 glass coverslips (catalog #106004-340, VWR). Slides were dried overnight at room temperature before imaging.

**Imaging.** Confocal images were acquired with a line-scanning confocal microscope (model LSM710, Zeiss) using a Zeiss Plan Apo 20×/0.8 objective and Multi-Alkali Photomultipliers, acquired at 16 bits with a spatial resolution of 3340 × 3440 pixels. Quantification of RS1 protein and mRNA signal was obtained using Fiji (NIH) following importation of native .czi files. For RS1 mRNA sections, which were acquired at multiple *z*-planes, an average intensity *z*-projection was applied to produce a single image from which signals were quantified. Immunohistochemistry signals were quantified from the raw, single *z*-plane, images.

Regions of interest (ROIs) were drawn at different retinal locations: ganglion cell layer (GCL; ~7660  $\mu\text{m}^2$ ), IPL (~960  $\mu\text{m}^2$ ), inner nuclear layer (INL; ~7223  $\mu\text{m}^2$ ), OPL (~114  $\mu\text{m}^2$ ), ONL (7480  $\mu\text{m}^2$ ), and inner segment (IS)/outer segment (113  $\mu\text{m}^2$ ). At earlier timepoints (P3 and P5), there is a single retinal layer termed the neuroblastic layer (NBL), and outer and inner nuclear layers have not yet formed into two distinct cell layers within the retina. However, even at these early timepoints, cells fated for the INL were localized to the anterior (closer to the vitreous) portion of the NBL (Takada et al., 2004). As such, at the early timepoints, the INL was sampled as the anterior portion of the NBL, whereas the ONL was sampled as the most posterior portion of the NBL. The OPL does not form until P7. For immunohistochemistry images, the OPL was sampled from P7 onward, and for RS1 mRNA images, from P9 onward. Mean pixel gray values within the ROIs were obtained and recorded. An additional large ROI (7024  $\mu\text{m}^2$ ) was drawn spanning the entire retina, and a plot of distance versus mean gray value was recorded to obtain a profile of RS1 protein or mRNA expression throughout the entire retina.

**Spectral-domain optical coherence tomography.** Imaging procedures have been described in detail previously (Bell et al., 2014, 2015). In brief, mice were anesthetized (sodium pentobarbital, 68 mg/kg) and pupils were dilated with 1  $\mu\text{l}$  of eyedrops composed of 0.5% tropicamide and 0.5% phenylephrine HCl. The corneal surface was anesthetized with a single application of ~10  $\mu\text{l}$  of 0.5% proparacaine. SD-OCT (Envisu R2210 UHR, Leica Microsystems) images of the retina were collected along the horizontal and vertical meridians centered on the optic disk. Each volumetric scan consisted of five B-scans (1000 A-scans per B-scan by 30 frames), which were coregistered and averaged using InVivoVue software (Leica Microsystems). Each B-scan was ~1.8 mm in width and had an axial resolution of 1.4  $\mu\text{m}$ .

### Optophysiology

**Tissue preparation.** 20 min before mice were killed by CO<sub>2</sub>, they were injected intraperitoneally with a solution of Evans Blue (Sigma-Aldrich); 50  $\mu\text{l}$  (33  $\mu\text{g}/\mu\text{l}$ ) for animals aged P10 to P22; and 150  $\mu\text{l}$  (66  $\mu\text{g}/\mu\text{l}$ ) for animals aged >P60. This compound adheres to the vascular lumen and fluoresces in response to a broad excitation spectrum with red-shifted emissions, allowing us to image blood vessels in a different channel than the green-emitting calcium dynamics of GCaMP. For all experiments, dissections were performed in a dark room, and the tissue was submerged in oxygenized HEPES-buffered extracellular Ringer's solution containing the following (in mM): NaCl 137, KCl 2.5, CaCl<sub>2</sub> 2.5, MgCl<sub>2</sub> 1.0, Na-HEPES 10, and glucose 28, at pH 7.4. During imaging,

retinal explants were superfused with carboxygenated Ames solution (Sigma-Aldrich).

Following enucleation, left eyeballs were immersed in buffered HEPES, pierced with a 26 gauge intradermal needle (Precision Guide at the interface between sclera and cornea, then sheared with Vannas scissors along this interface just below the ora serrata. Retinas were separated from the eyecups by gently pulling on the vitreous with Dumont #5 forceps, and then sheared in three or four equitable "slices" with Vannas scissors. The remaining vitreous humor was removed from the surface of the retina without touching the neural tissue. Individual explants were mounted GCL-up on filter holders (as described previously; Ivanova et al., 2013), then incubated in a humidified chamber for 2–3 h while submerged in buffered HEPES.

**Acquisition.** GCaMP fluorescence fluctuations were imaged on an upright two-photon microscope (model Bergamo II, Thorlabs) with a 16× physiological objective (Nikon) and a multiphoton excitation set at 920 nm. The light path enabled a separation of red and green fluorescence at two concurrent photomultiplier tubes, or green fluorescence with concurrent retinal photoreceptor stimulation with a lime LED (550–575,  $\lambda$  max 565 nm; model M565L3, Thorlabs). During imaging, the retina was superfused with bicarbonate-buffered Ames solution that was constantly equilibrated with 95% O<sub>2</sub> and 5% CO<sub>2</sub> and temperature controlled at 32°C with an inline heater (model TC-334, Warner Instruments) controlled by a thermocontroller (model TC-344B, Warner Instruments). Each explant was imaged at the mediolateral region.

**Live *z*-stack imaging.** Image acquisitions were performed with ThorImage 3.2 (Thorlabs) and saved as Bio-Format TIFF folders (Open Microscopy Environment). The piezo-driven microscope stage enabled acquisition at 1  $\mu\text{m}$  spatial resolution in *Z* at a spatial resolution of 1024 × 1024 pixels, with unidirectional scanning and 5× frame averaging. Data were imported and processed in Fiji (NIH) before exporting as .csv files for further processing using custom MATLAB scripts.

**Dynamic signal acquisition.** Image acquisitions were performed with ThorImage 3.2 (Thorlabs) and saved as 16 bit unsigned TIFF-stacks. Single-plane acquisition (spontaneous signals) was performed at a spatial resolution of 1024 × 1024, a magnification of 16×, a spatial resolution of 0.815  $\mu\text{m}/\text{pixel}$ , and a temporal resolution of 1.53 frames/s (fps; 7.65 fps with 5× frame averaging). Multiplane acquisition (Fast-*Z*) was performed with a galvo-resonant scanner (8 kHz), with five to seven planes spaced 20  $\mu\text{m}$  from each other at a spatial resolution of 512 × 512 pixels and magnifications of either 32× (1.63 pixels/ $\mu\text{m}$ ) or 64× (3.26 pixels/ $\mu\text{m}$ ) at a final temporal resolution of 1.975 fps.

**Light stimulation.** Light stimulation was controlled by ThorSync 3.2, which mediated illumination and the extinction of the stimulation LED by means of TTL (transistor–transistor logic) signals at a sampling frequency of 30 kHz. Three light stimulation protocols were used: five repeats of 1 s ON/4 s OFF; 20 repeats of 500 ms ON/500 ms OFF; and five repeats of 10 s ON/120 s OFF. Light stimulation was initiated after a 30 s period of adaptation to the illumination provided by the multiphoton calcium imaging system. Irradiance at the retinal sample was measured with a spectroradiometer (model ILT950, Information Light Technologies), and derived using Govardovskii nomograms (Govardovskii et al., 2000; Allen et al., 2014). Isomerizations estimates for the stimulating LED were  $6.16 \times 10^{12}$  (m-cone opsin),  $7.27 \times 10^{10}$  (s-cone opsin),  $4.31 \times 10^{12}$  (rod opsin), and  $1.7 \times 10^{12}$  (melanopsin) photons/cm<sup>2</sup>/s.

**Pharmacology.** The pharmacological compounds (with final concentration and vendor) used in this study were AP4 (2-amino-4-phosphonobutyric acid; 20  $\mu\text{M}$ ; Tocris Bioscience), AP5 (aminophosphonopentanoic acid; 50  $\mu\text{M}$ ; Tocris Bioscience), CNQX (6-cyano-7-nitroquinoxaline-2,3-dione; 10  $\mu\text{M}$ ; Tocris Bioscience), ouabain (10  $\mu\text{M}$ ; Sigma Aldrich); and TBOA (DL-threo- $\beta$ -benzyloxyaspartate; 25  $\mu\text{M}$ ; Tocris Bioscience). These were diluted in bicarbonate-buffered Ames solution, continually equilibrated with 95% O<sub>2</sub> and 5% CO<sub>2</sub>. When studying glutamatergic blockade, an explant was subjected to three blockers (CNQX, AP5, and AP4), which were applied in a random order for each experiment. Pharmacological investigations consisted of the last step in optophysiological imaging for an explant, and the entire perfusion system was cleaned with 70% ethanol and distilled water between explants.

←

layers. The *z* profile of GCaMP6f fluorescence from six KO retinas displays a stunted distribution, with no clear peaks. The gray legend between control and KO plots provides a rough guide to retinal layers according to depth from GCL surface. non-significant (ns)  $p > 0.05$ , \* $p \leq 0.05$ .



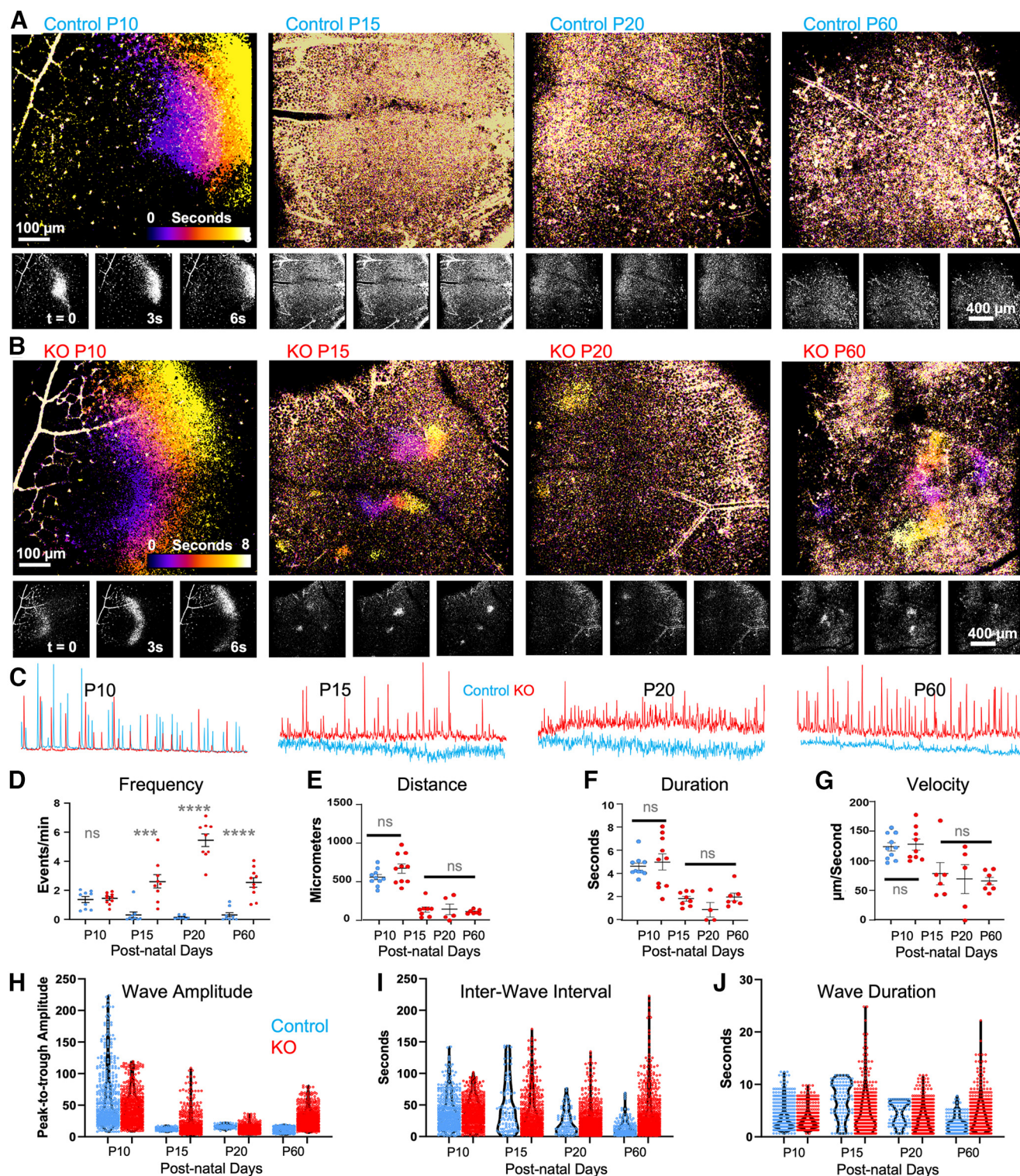
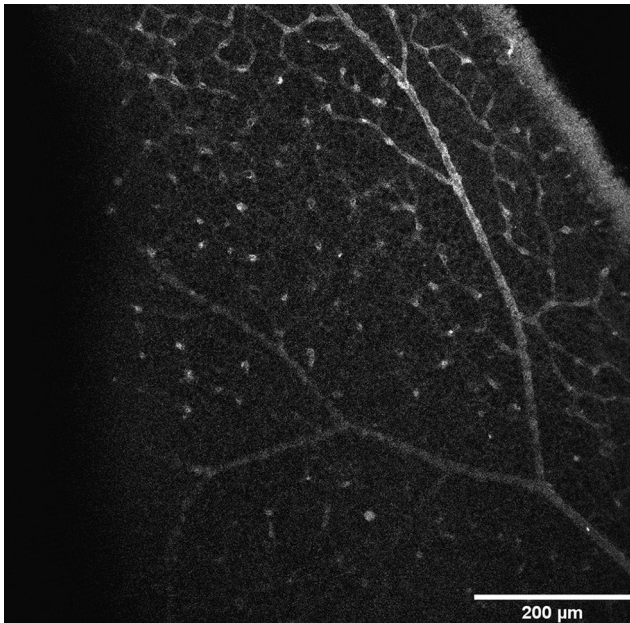
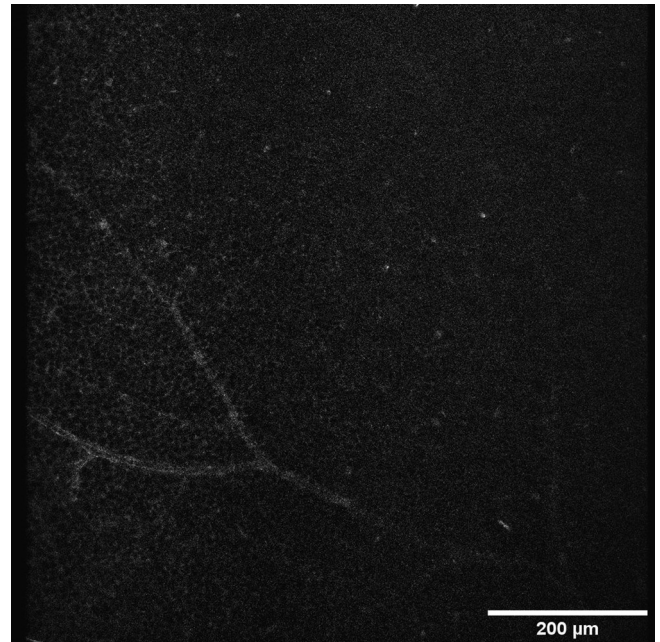


**Figure 3.** Progressive divergence of spontaneous neuronal activity during retinal maturation. **A**, Representative propagation profiles of P10, P15, P20, and P60 control retinas. While developmental neural waves were observed in controls at P10, they were not seen at later ages. **B**, The developmental neural waves seen at P10 persisted at later ages in KO retinas. The three panels at the bottom display still images at key temporal points. **C**, Representative fluorescence signal traces from 100  $\times$  100 pixel ROIs for each genotype at each age. **D**, Number of spontaneous events/min/explant, averaged over five ROIs.  $N = 11$  (P15 control),  $N = 8$  (P15 KO),  $N = 10$  (P20 control),  $N = 8$  (P60 control), and  $N = 12$  (P60 KO) from six mice per condition. **E–G**, Average distance (**E**), duration (**F**), and velocity (**G**) for five waves/explant. Mann–Whitney test with multiple comparisons yielded  $p$  values of 0.999 (**D**, frequency), 0.7546 (**E**, average distance per explant), 0.616 (**F**, average duration per explant), and 0.842 (**G**, average velocity per explant). For frequency, the Mann–Whitney test with multiple comparisons yielded  $p$  values of 0.0002 (P15;  $N = 11$  control explants and  $N = 15$  KO explants),  $<0.0001$  (P20;  $N = 10$  control explants and  $N = 11$  KO explants),  $<0.0001$  (P60;  $N = 8$  control explants and  $N = 12$  KO explants). Mann–Whitney tests yielded  $p$ -values of 0.357 (**E**, average distance per explant), 0.877 (**F**, average duration per explant), 0.3680 (**G**, average velocity per explant). **H–J**, Violin plot distributions of neural wavelet amplitude (**H**), interwave interval (**I**), and duration (**J**), displaying individual values for each wavelet detected. non-significant (ns)  $p > 0.05$ , \*\*\* $\leq 0.001$ , \*\*\*\* $\leq 0.0001$ .

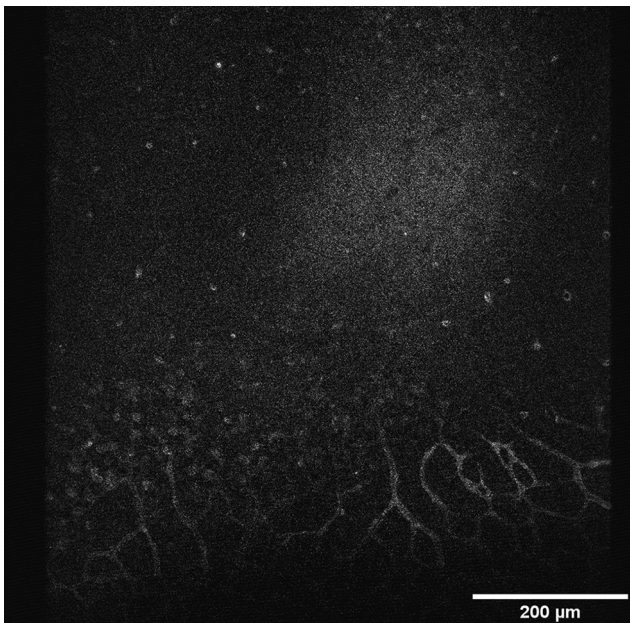




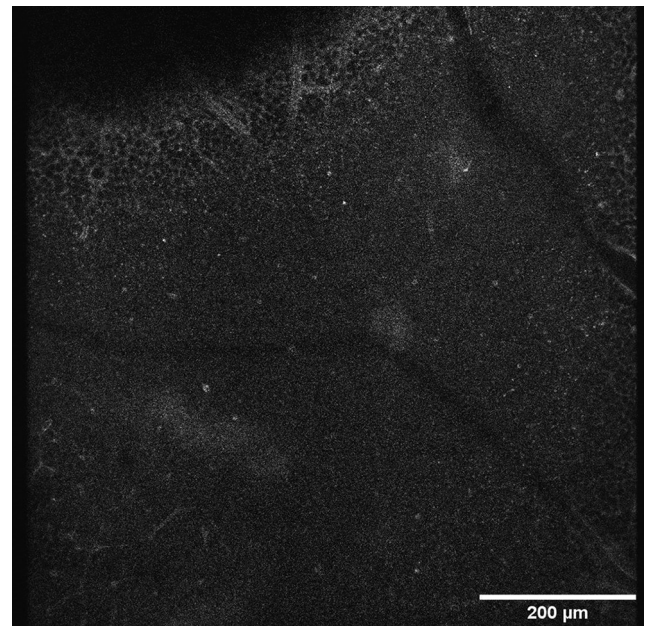
**Movie 1.** Spontaneous retinal activity in control GCaMP6f mice at P10. [View online]



**Movie 3.** Spontaneous retinal activity in control GCaMP6f mice at P15. [View online]



**Movie 2.** Spontaneous retinal activity in Rs1 KO GCaMP6f mice at P10. [View online]



**Movie 4.** Spontaneous retinal activity in Rs1 KO GCaMP6f mice at P15. [View online]

#### Exclusion criteria

For optophysiology, retinas yielded at least two explants, each of which underwent the entire acquisition protocol described above. The data from some recordings were unusable because of recording artifacts that stemmed from mechanical drift, perfusion pump failure, microscope failure, or light stimulation errors. The protocol was repeated if the failure was observed online. In cases where it was not, the specific recording was excluded, but other recordings from the same explant were retained. As such, each experiment used a minimum  $N = 5$  animals, although the number of explants varied.

#### Image processing

*For quantitative analyses of spontaneous calcium dynamics.* Spontaneous calcium dynamics were measured at a magnification of  $16\times$  during 11 min recordings, recorded in a single plane and sampled at 1.53 fps, with online averaging of 5 frames. Neural and vascular

structures were readily identifiable from observations of each frame, since they had exhibited strong resting fluorescence at all ages and phenotypes. Glial structures were detected manually by observing each frame of a video recording, because they only appeared in bright, sporadic bursts. Five neural ROIs were chosen from pseudo-random positions of the visual field, avoiding vascular structures. The raw fluorescence signal for each ROI was extracted in Fiji (NIH), then exported to MATLAB as .csv files and processed with custom scripts. Fluorescent signals ( $F$ ) were normalized ( $\Delta F/F$ ) by the following formula:

$$\Delta F/F = \frac{F - \mu F}{\sigma F},$$

with  $\mu F$  and  $\sigma F$  corresponding to the mean and SD of the fluorescence over each pixel within an ROI and over the entire time series for each recording.



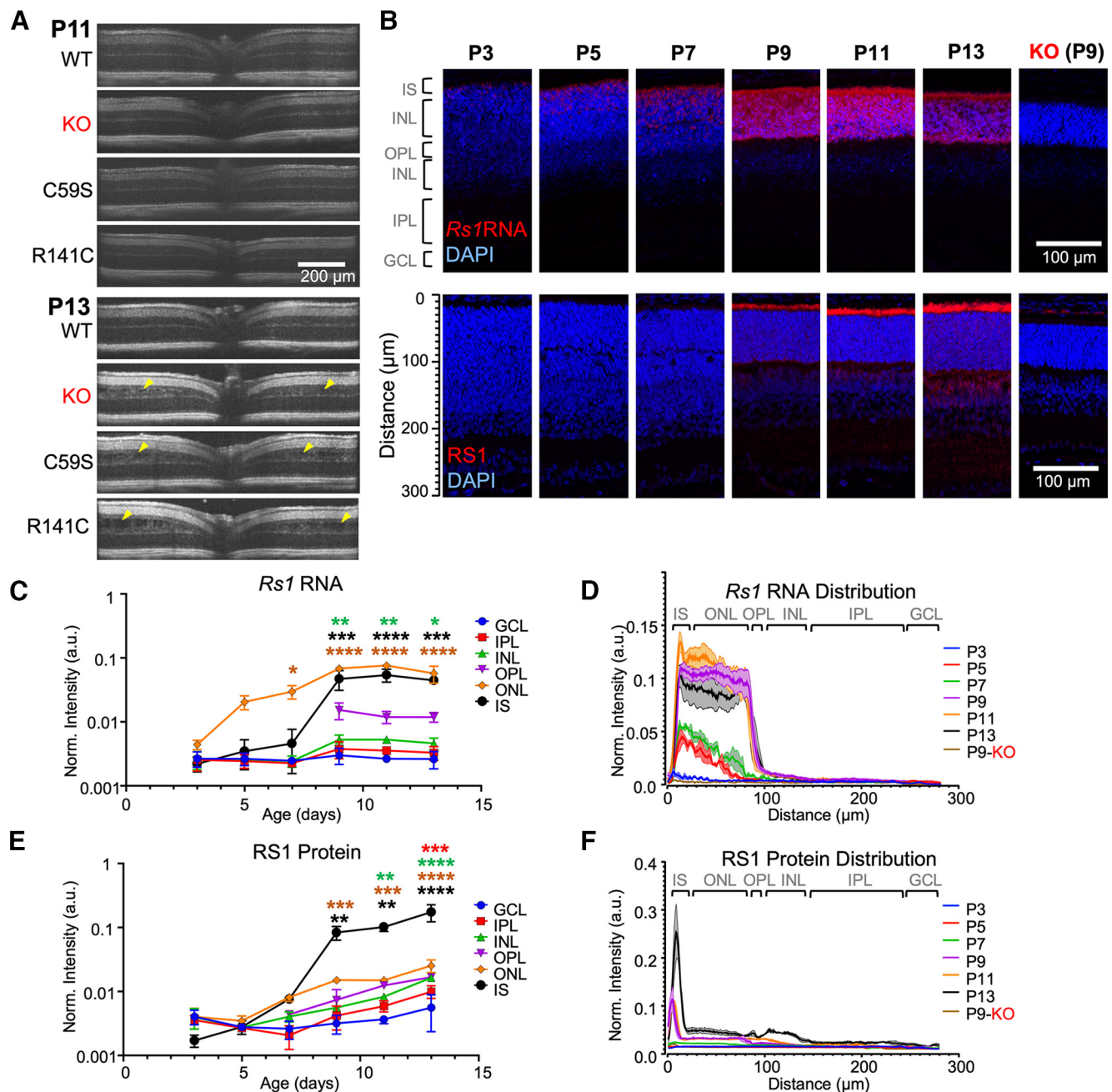


**Figure 4.** RS1 expression precedes the appearance of schisis during development. **A**, OCT imaging of three RS1-deficient mouse models at P11 and P13. At P11, the XLRS models are indistinguishable from the control retina. Schisis appears at P13 in (yellow arrowheads). **B**, Retinal sections stained for nuclei (DAPI, blue), Rs1 RNA (red, top), and RS1 protein (red, bottom). **C**, **E**, Fluorescence intensity in the red channel for Rs1 RNA (**C**) and RS1 protein (**E**) in different layers of the retina. One-way ANOVA with multiple comparisons for each retinal layer compared with P3,  $N = 3$  mice per condition. For **C**,  $p = 0.0023$ ,  $0.0024$ ,  $< 0.0001$  (INL at P9, P11, and P13, respectively);  $p = 0.0195$  at P7;  $p < 0.0001$  at P9, P11, and P13 (ONL);  $p = 0.0002$ ,  $p < 0.0001$ , and  $p = 0.0003$  (IS at P9, P11, and P13, respectively). For **E**:  $p = 0.003$  (IPL);  $p = 0.0011$  and  $p < 0.0001$  (INL at P11 and P13, respectively);  $p = 0.0008$ ,  $p = 0.0008$ ,  $p < 0.0001$  (ONL at P9, P11, and P13, respectively);  $p = 0.0052$ ,  $p = 0.0011$ , and  $p < 0.0001$  (IS at P9, P11, and P13, respectively). **D**, **F**, Normalized mean fluorescence ( $\pm$  SEM) intensity profiles through retinal cross sections from the edge of photoreceptor inner segments in the red channel for Rs1 RNA (**D**) and RS1 protein (**F**). non-significant (ns)  $p > 0.05$ , \*  $p \leq 0.05$ , \*\*  $p \leq 0.01$ , \*\*\*  $p \leq 0.001$ , \*\*\*\*  $p \leq 0.0001$ .

Waves and wavelets were thresholded with  $4 \times$  SDs over a sliding average. Wavelet metrics (peak-to-trough amplitude, interwave interval, wave duration) were exported and plotted as distributions or averaged by wave, ROI, explant, and animal for each condition using the formula below:

$$\text{AvgMetric} = \frac{1}{n\text{Animals}} \sum_{i=1}^{n\text{Animals}} \frac{1}{r\text{Exp}} \sum_{j=1}^{r\text{Exp}} \frac{\sum_{k=1}^{w\text{ROI}} \text{metric}}{w\text{ROI}},$$

where  $n\text{Animals}$  corresponds to the number of animals per condition,  $r\text{Exp}$  corresponds to the number of ROIs per explant (five, for neuronal

and vascular signals), and  $w$  corresponds to the number of waves detected in each ROI. Propagation distance and velocity were calculated manually in Fiji (NIH) for five events/explant/animal.

The correlation coefficient matrix for five neuronal and five vascular ROIs was calculated in MATLAB before removing the diagonal auto-cross-correlation coefficients and averaging the neuro-neuro, neuro-vascular, and vascular-vascular cross-correlation coefficients of those five ROIs for each explant.

**For pharmacological experiments.** All pharmacological experiments were performed with six-plane multilayered imaging, and two fly-back frames. For neuronal signals, an ROI of  $100 \times 100$  was applied manually



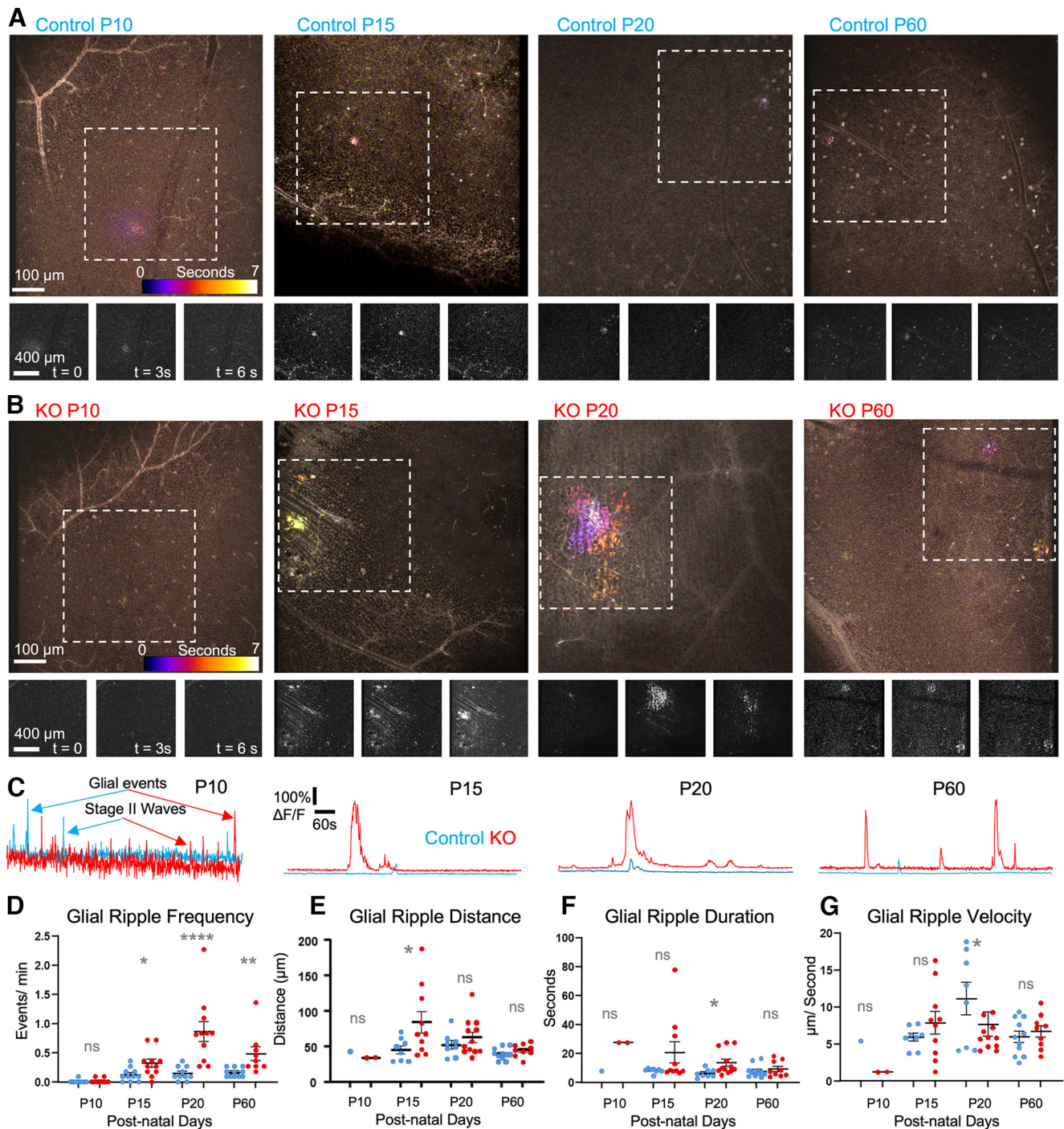


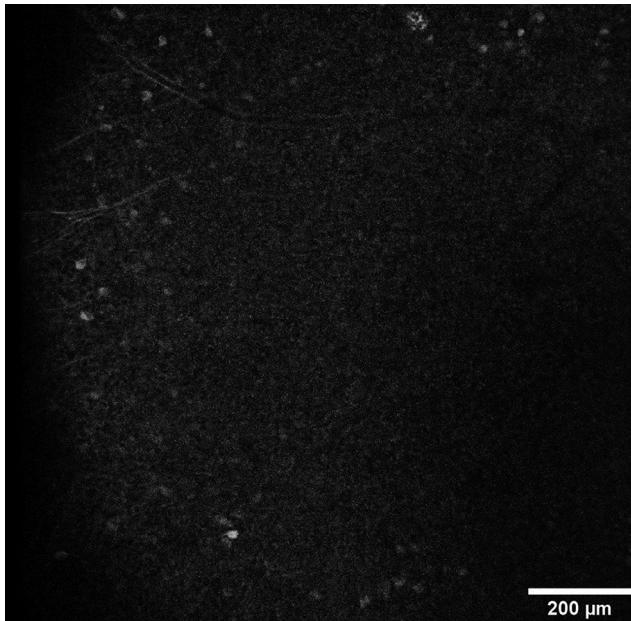
**Figure 5.** RS1-deficient retinas display aberrant spontaneous glial signals after P15. **A, B**, Spontaneous glial ripples at GCL of control (**A**) and KO (**B**) retinal explants, for each age examined. The three panels at the bottom display still images at key temporal points of the glial ripple. **C**, Example fluorescence traces for both genotypes at key developmental stage. **D**, Frequency of spontaneous glial ripple per explant. **E–G**, Statistical metrics for glial events including velocity (**E**), duration (**F**), and distance (**G**) for a maximum five events per explant.  $N = 11$  (P15 control), 8 (P15 KO), 10 (P20 control), 11 (P20 KO), 8 (P60 control), and 12 (P60 KO) from six mice per condition. **D**, After eye opening, using a Mann–Whitney test with multiple comparisons, the  $p$ -values at each age when comparing genotypes were 0.028 (P15;  $N = 11$  WT explants and 15 KO explants),  $<0.0001$  (P20;  $N = 10$  control explants and 11 KO explants), and 0.0014 (P60;  $N = 8$  control explants and 12 KO explants). Mann–Whitney tests yielded  $p$ -values of 0.005 (**E**, distance, P15), 0.058 (**E**, distance, P20), 0.1944 (**E**, distance, P60), 0.646 (**F**, duration, P15), 0.0151 (**F**, duration, P20), 0.710 (**F**, duration, P60), 0.332 (**G**, velocity, P15), 0.024 (**G**, velocity, P20), and 0.537 (**G**, velocity, P60). non-significant (ns)  $p > 0.05$ ,  $*p \leq 0.05$ ,  $**p \leq 0.01$ ,  $****p \leq 0.0001$ .

to an area within a neural field where wavelets were clearly observed. The raw fluorescence signal was extracted in Fiji (NIH), then exported to MATLAB as .csv files and processed with custom scripts that detected wavelets using unbiased thresholding (sliding average +  $4 \times$  sliding SD), then evaluated their frequency and amplitude for each retinal layer and for each pharmacological condition. Glial events were evaluated in a similar manner, with the exception that a new ROI was generated

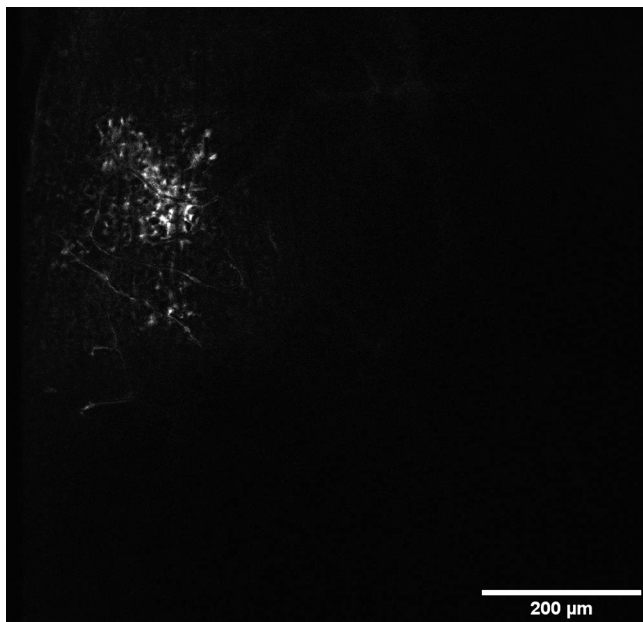
manually for each glial event, and metrics included the surface of glial propagation.

**Of multiphoton data for publication format.** For videos, files were imported into Fiji (NIH), and then averaged in groups of four images along the temporal axis. Brightness and contrast were balanced manually to optimize calcium signals. Videos were saved as Jpeg-compressed .avi files, with a frame rate of 8 fps. This resulted in an effective frame rate of





**Movie 5.** Spontaneous retinal activity in control GCaMP6f mice at P60. [View online]



**Movie 6.** Spontaneous retinal activity in Rs1 KO GCaMP6f mice at P20. [View online]

24 fps, corresponding to an accelerated display speed of approximately 16×. For temporally projected still images, stacks were processed in Fiji (subtracted background, Gaussian blur) before manual thresholding. Further binary processing was necessary to highlight waves or wavelets before projection of the temporal hyperstack using the Fiji “Fire” lookup table.

#### Whole-mount IHC.

Labeling of glutamine synthetase (GS) in the retina highlights MCs, while glial fibrillary acidic protein (GFAP) highlights astrocytes and immune-responsive Müller cells; a subset of retinal ganglion cells (RGCs) expresses SMI-32. The primary antibodies used in this study were as follows: goat anti-mouse albumin (1:800; catalog #A90-234A, Bethyl; RRID:AB\_67122); mouse anti-GS (1:2000; catalog #MAB302, Millipore); chicken anti-GFAP (1:3000; catalog #AB5541, Chemicon;

RRID:AB\_177521); and mouse anti-SMI-32 (1:2000; catalog #SMI-32R, Covance); and Hoechst 33342 (1:300; Sigma-Aldrich) for nuclear labeling. The secondary antibodies were conjugated to Alexa Fluor 488 (1:1000; green fluorescence; Thermo Fisher Scientific), Cy3 (1:500; red fluorescence; Jackson ImmunoResearch), and Cy5 (1:500; far red fluorescence; Jackson ImmunoResearch). Following optophysiological experiments, explants were fixed in a solution of 4% PFA in PBS for 15 min. After fixation, explants were washed three times for 15 min in PBS, then blocked for 10 h in CTA, a PBS solution containing 5% chemiblocker (membrane-blocking agent; Chemicon), 0.5% Triton X-100, and 0.05% sodium azide (Sigma-Aldrich).

Primary antibodies were diluted in CTA and incubated for 72 h, followed by incubation for 48 h in the appropriate secondary antibody and nuclear stain. After staining, explants were flat mounted on a slide, GCL up, and coverslipped using Vectashield mounting medium (catalog #H-1000, Vector Laboratories). The coverslip was sealed in place with transparent nail varnish. To avoid compression of retinal explants, small pieces of glass coverslips (1 mm thick) were placed in the space between the slide and the coverslip on either side of each explant. All steps were completed at room temperature, except for incubation of the GS primary antibody, which required a 37°C incubation while being gently shaken. Slides were imaged in an upright confocal microscope (model SP8, Leica) or inverted confocal microscope (model A1R HD25, Nikon). Data were imported and processed in Fiji (NIH) using custom-written macros.

#### Optokinetic tracking.

Spatial frequency thresholds for optokinetic tracking of sine-wave gratings were measured using a virtual optokinetic system (OptoMotry, CerebralMechanics), as described in the original study (Prusky et al., 2004), and more recently in the study by Alam et al. (2022). Five littermates of each *NG2 GCaMP6f<sup>+/−</sup>* (control) and C57BL/6J mouse were tested repeatedly after retinal maturation (postnatal days 21–94).

#### Statistics.

Statistical analyses and graph generation were performed in Prism (versions 8.2 and 9.1.0; GraphPad Software) for *RS1* expression analyses. The Mann–Whitney test was used for comparing nonparametric datasets in groups of two. The Kruskal–Wallis test with Dunn’s multiple-comparisons test was used to compare groups of three or more nonparametric datasets. *Rs1* expression analyses were analyzed using one-way ANOVA for each retinal layer with Dunnett’s multiple-comparisons test.

## Results

### Generation and validation of a reporter system for the unbiased characterization of neuroglial dynamics

The intracellular calcium dynamics of retinal cells was characterized in the absence or presence of *RS1*. This was accomplished by generating a mouse line that expresses the fast intracellular calcium indicator GCaMP6f (Chen et al., 2013) in most retinal cell types (neurons, glia, and vascular cells) via crossing two commercially available transgenic lines (Fig. 1A). The *NG2 Cre* mice [B6;FVB-Tg(Cspg4-cre) 1Akik/J; catalog #008533, The Jackson Laboratory] express *Cre recombinase* under the control of the mouse chondroitin sulfate proteoglycan 4 [*Cspg4*; also known as *Neuro-Glia 2* (*NG2*)] promoter, resulting in early embryonic *Cre* expression in CNS glial, vascular, and neuronal cells (Zhu et al., 2008). Note that the *NG2* promoter is only active in contractile vascular cells during adulthood (Zhu et al., 2008). The floxed GCaMP6f mice [B6].Cg-Gt(*ROSA*)26Sortm95.1(CAG-GCaMP6f)Hze/MwarJ; catalog #028865, The Jackson Laboratory] have the GCaMP6f construct downstream of the ubiquitous CAG promoter and a stop sequence flanked by loxP sequences, resulting in strong *GCaMP6f* expression by cells also expressing *Cre recombinase*. The resulting offspring (*NG2 GCaMP6f*) persistently express



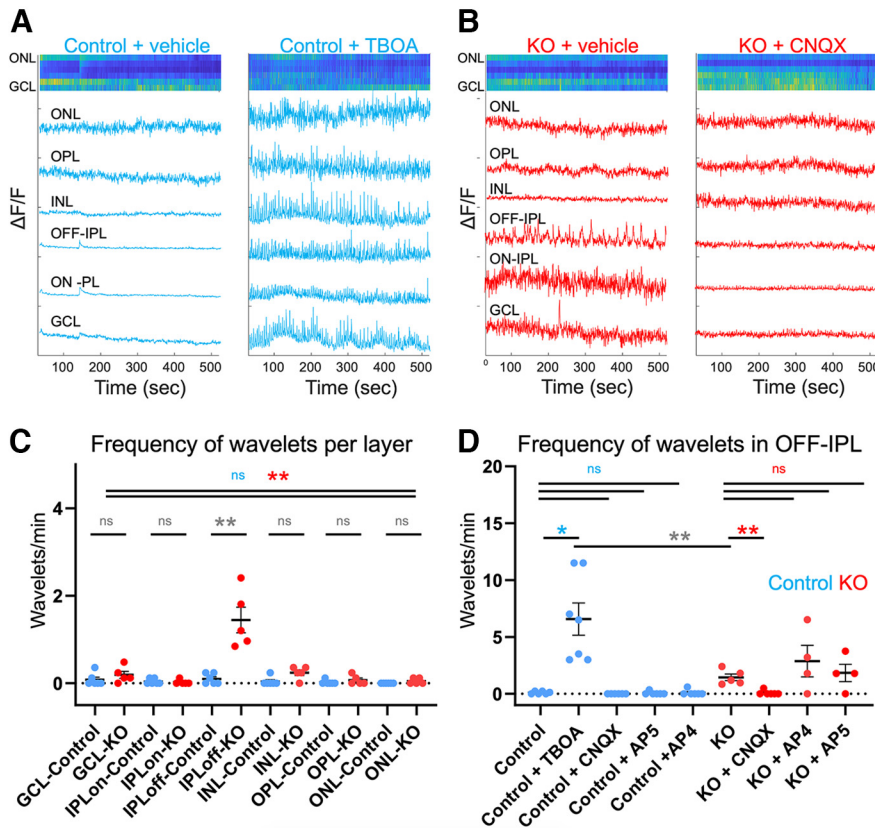


**Figure 6.** Neural wavelets originate in the OFF-IPL and are driven by glutamate in the mature retina. **A, B**, Example traces from 9 min recordings of spontaneous activity using FastZ imaging in six retinal layers simultaneously in mature control (**A**) and KO (**B**) explants. The ionotropic glutamate receptor blocker CNQX abolished spontaneous wavelets in the OFF-IPL of KO retinal explants (**B**), but the glutamate transport blocker TBOA induced spontaneous signals in control retinas (**A**). **C**, Wavelet frequency was highest in the OFF-IPL layer of KO retinas and was completely absent from control retinas.  $N = 5$  for each genotype. Mann–Whitney test,  $N = 10$  animals, 5 per genotype,  $p = 0.0025$  for IPL-OFF. **D**, Wavelet frequency in the OFF-IPL of control retinas was increased by the application of TBOA. Wavelet frequency in the OFF-IPL of KO retinas was reduced by the application of CNQX, but not AP4 or AP5. Friedman test with repeated measures,  $N = 7$  (control + TBOA,  $p = 0.0458$ ),  $N = 5$  (control + CNQX,  $p = 0.0005$ ; and RS + CNQX,  $p = 0.0043$ ),  $N = 4$  (control + AP4,  $p = 0.0041$ ; KO + AP4,  $p = 0.5556$ ),  $N = 4$  (control + AP5,  $p = 0.0036$ , KO + AP5,  $p = 0.8571$ ). non-significant (ns)  $p > 0.05$ ,  $** \leq 0.01$ .

the calcium indicator in all CNS neural, vascular, and glial cells (including the retina). We interbred these mice until a fully homozygous line was obtained (*NG2 GCaMP6f*). We then crossed *NG2 GCaMP6f* homozygous males with homozygous KO females lacking *Rs1*, resulting in male offspring that were heterozygous for *NG2 GCaMP6f* and lacked *RS1* (*NG2 GCaMP6f*<sup>+/+</sup>; *Rs1*<sup>−/−</sup>). As the *Rs1* gene resides on the X chromosome (Sauer et al., 1997), these male mice, hereafter referred to as KO, exhibited the phenotype observed in *Rs1* mutants including retinal schisis, which was visible in our *ex vivo* configuration (Liu et al., 2019). To monitor calcium dynamics in age-matched and sex-matched control animals, we crossed *NG2 GCaMP6f*<sup>+/+</sup> mice with the C57BL/6J line.

We used live *ex vivo* multiphoton imaging to record simultaneously from different depths of the retina. Our methodology enabled the concurrent imaging of physiological processes with GCaMP (green) and three-dimensional navigation of retinal explants via the Evans blue labeling of the vascular lumen (Fig. 1B, red). This generated an enduring demarcation of the recording zone to enable the alignment of IHC for *post hoc* analyses. Individual neuronal cell bodies were readily observable in the retinal nuclear layers, as can be seen in the GCL of a representative retina in Figure 1, C and D. Many cells responded to 565 nm light stimulation with ON, OFF, or ON-OFF fluorescence

profiles. In Figure 1E, traces correspond to an example OFF RGC (gray arrowhead) and ON RGC (blue arrowhead) from Figure 1C. Endothelial cells, pericytes, and smooth muscle cells were also readily identifiable around blood vessels by their morphology as they displayed strong baseline fluorescence. The processes of MCs and astrocytes were observable between neurons and around vascular structures, yet were only identifiable when they displayed strong sporadic bursts of fluorescence (Figs. 1H, 2A,B). Indeed, the live activation profile of GCaMP fluorescence in MCs is evident in a 90° 3D projection of a static *z* stack performed during the occurrence of such a burst of activity (Fig. 1H). We confirmed the ubiquitous expression of GCaMP in MCs using IHC on both KO and control retinas by demonstrating the colocalization of expressed GCaMP6f and the protein GS (Fig. 2C,D). After fixation, MCs and vascular structures presented a stronger fluorescence signal than did neurons or astrocytes. We further confirmed the ubiquitous expression of GCaMP in neurons by comparing the fraction of round (neuronal) minus elongated (vascular) fixed nuclei in the GCL to the total number of live GCL cells depolarized by the Na<sup>+</sup>/K<sup>+</sup>-ATPase blocker ouabain (Fig. 1F,G). To evaluate the potential toxicity of expressing GCaMP6f in all cells of the retina, we compared the macroglial reactivity of NG2 GCaMP and NG2 GCaMP *Rs1*<sup>−/−</sup> retinas with C57BL/6J retinas. We found that C57BL/6J and NG2 GCaMP control mice did not differ significantly (Fig. 2E,F). Using optokinetic tracking, we also established that the behaviorally assessed photopic visual function of C57BL/6J and control animals was similar (Fig. 1I). Dynamic green fluorescence was expressed throughout development and into adulthood for control and KO mice in neuronal, vascular, and glial cells (Fig. 2A,B).

### Abnormal neural “wavelets” appear at eye opening

We monitored spontaneous and light-driven calcium dynamics using multiphoton calcium imaging in *ex vivo* retinal explants (see Materials and Methods) at ages that correspond to key stages of visual development: P10 to P11, P14 to P15, P20 to P22, and P60 to P90.

Stage II developmental waves are an important feature of retinal development, refining lateral cholinergic synapses between RGCs and amacrine cells (ACs) of the GCL (Feller et al., 1996). Figure 3, A and B, displays representative Stage II waves at P10, each occurring across an 8 s recording epoch and covering >500 μm. For P10 control mice, the pseudocolor scale shows coordinated rightward propagation in time from 0 s (blue) to 7.5 s (white). To highlight the propagation profile of coordinated waves of activity, the pseudocolor plot is segmented into three monochrome snapshots in time within the 8 s of activity, at time 0, 3, and 6 s below the large pseudocolor plot, for each age. In

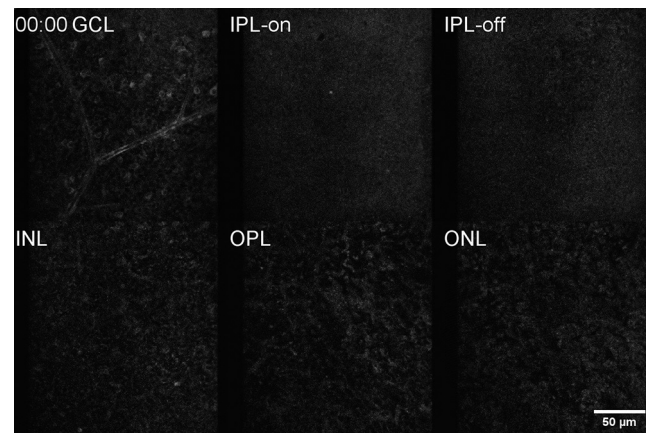
contrast, Figure 3B shows coordinated propagation in the KO mice at all ages. Figure 3C compares normalized fluorescence in control and KO mice over time, for a representative ROI at each of four ages. Figure 3D–G displays summary metrics (frequency, distance, duration, and velocity) for the waves recorded in each explant at these ages. Spontaneous events recorded at P10 exhibited frequency, velocity, duration, and interwave intervals typical of Stage II retinal waves (Demas et al., 2006; Maccione et al., 2014), which did not differ significantly between the control and KO mice with respect to any parameter (Fig. 3D–G, Movies 1, 2).

At later ages, KO retinas exhibited a previously unobserved phenomenon, which we termed “wavelets”: transient lateral propagation along the neuronal field (Fig. 3B,C, Movies 3, 4). To characterize this, we applied metrics typically used for the study of retinal developmental waves (interwave interval distribution, duration, frequency, velocity, and distance traveled; Demas et al., 2006; Maccione et al., 2014). We initially analyzed large portions of the retina ( $16\times$  magnification,  $734 \times 834 \mu\text{m}$ ) to ensure that the phenomenon was not restricted to isolated locations, such as cystic cavities. To maximize reproducibility, for each explant we analyzed five different ROIs. Each ROI was  $100 \times 100$  pixels ( $122.6 \times 122.6 \mu\text{m}$ ) and was chosen pseudorandomly during *post hoc* analysis with the sole criteria that the ROI was devoid of visible vasculature.

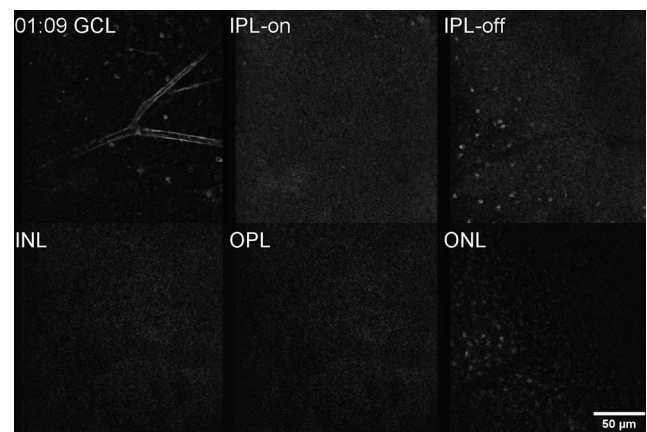
After eye opening, waves stopped in control retinas, as shown previously (Feller et al., 1996; Feller, 2009; Maccione et al., 2014), but persisted as wavelets in KO retinas. Figure 3, B and C, displays several examples of these occurring over an 8 s period. Although these events were more frequent (Fig. 3D), they were shorter, slower, and smaller than Stage II waves seen at P10 (Fig. 3E–G). The average distance, duration, and velocity of KO wavelets did not differ significantly among age groups (Fig. 3E–G). The individual values for the amplitude, interwave interval and durations are plotted as violin distributions (Fig. 3H–J), revealing comparable profiles across age groups.

Based on the observation that the disease phenotype is manifest in *Rs1* mutants as early as P13 to P15 (Fig. 4A; Liu et al., 2019), we further characterized the time course for *Rs1* expression and RS1 distribution using *RNAscope* and IHC on retinal sections from mice aged P3, P5, P7, P9, P11, and P13 (Fig. 4B–F). *Rs1* mRNA transcription is first observed at P5, with a gradual increase throughout development. RS1 protein is first clearly detected at P9, in the photoreceptor inner segments as well as in the developing OPL, with a subsequent age-dependent increase in the inner segments and throughout the retina. Because RS1 is a secreted protein that can move in the extracellular space, absolute registration between the location of the protein and the location of its synthesis by RNA was not expected.

Next, we examined the developing retina with respect to a key feature of the *Rs1* mutant phenotype: the presence of cavities on OCT imaging. Figure 4A compares representative OCT images of control and *Rs1* mutant retina at P11 and P13, the time between when RS1 protein is restricted to photoreceptors and then is present throughout the retina. At P11, the phenotype of *Rs1* mutant mice is indistinguishable from control; all retinal layers are present, and there is no evidence of schisis. By P13, schisis is observed in each *Rs1* mutant model. We previously showed that retinal schisis progresses further to a more severe phenotype at P15 (Liu et al., 2019). In view of the similarity between the phenotypes of the three *Rs1* mutant lines, we further studied this time window using optophysiological analysis of the GCaMP reporter line crossed to the KO line. We chose the KO as a representative XLRS model to provide reproducible



**Movie 7.** FastZ projections of retinal activity across retinal layers in P60 *Rs1* KO GCaMP6f mice. [View online]



**Movie 8.** FastZ projections of retinal activity in P61 control GCaMP6f following application of TBOA. [View online]

comparison points with existing and future literature, since various *Rs1*-null mutants have been developed and analyzed by multiple laboratories (Weber et al., 2002; Zeng et al., 2004; Jablonski et al., 2005).

### Abnormal glial phenotype

At P10, control and KO retinas had comparable morphology, which is commensurate with the consistency of spontaneous neural dynamics. In comparison, older KO retinas displayed many abnormalities in addition to the cystic structures that develop and characterize the disease phenotype (Liu et al., 2019). Some of those abnormalities were observed as fibrous structures in the plexiform layers (Fig. 2G). These may be because of reactive MCs, which upregulate GFAP in *Rs1* mutant mice (Liu et al., 2019), and many other retinal conditions (Yu et al., 2004; Gargini et al., 2007; Hippert et al., 2015). Alternatively, this abnormal distribution may be because of cystic cavities, a characteristic trait of the *Rs1*-deficient retina (Fig. 4A). In advanced photoreceptor degenerations, MCs are known to drive outer retinal remodeling, displaying hypertrophy, hyperplasia, phagocytosing dead photoreceptors, and colonizing the subretinal space (Jones et al., 2005, 2012). Using live *z*-stack imaging, we characterized the fluorescence depth profile through a  $150 \mu\text{m}$  retinal column within a pseudorandomly allocated surface (avoiding vasculature in all layers) of  $100 \mu\text{m}^2$  for six control and six KO



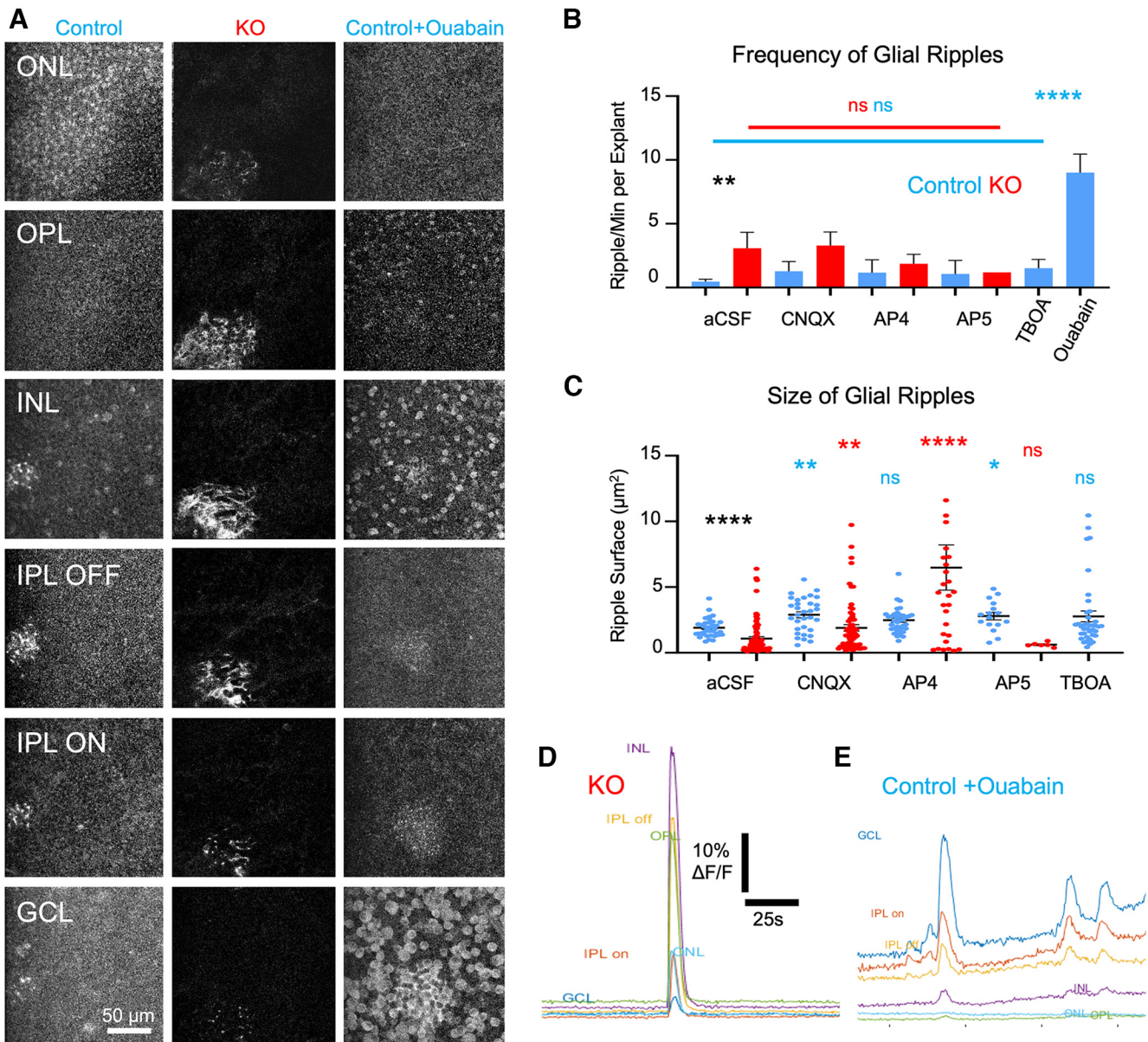
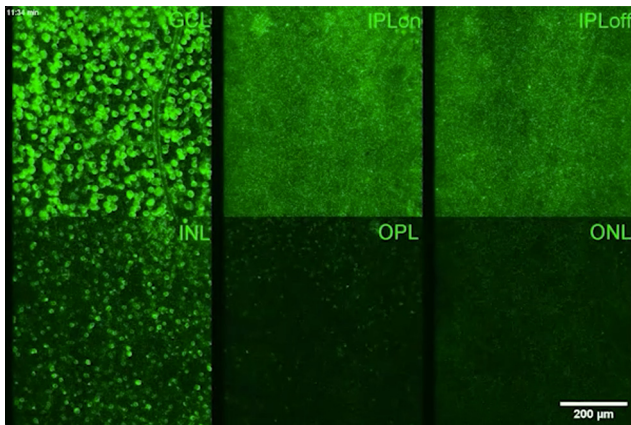


**Figure 7.** Spontaneous glial events occurred throughout the retina and can be modulated pharmacologically in the mature retina. **A**, Example spontaneous (control, KO) and induced (control + ouabain) glial events within all layers of the retina at P60, projected over 40 s. **B**, Throughout retinal layers, the frequency of glial ripples in KO retinas was significantly higher than that in control retinas (Mann–Whitney test,  $p = 0.0052$ ,  $N = 16$  control and 11 KO explant, aCSF KO vs control). Glutamate blockers did not modulate the frequency of glial ripples in either control (Kruskal–Wallis test,  $p = 0.1830$ ,  $N = 6$  explants/retina/condition) or KO retinas (Kruskal–Wallis test,  $p = 0.8989$ ,  $N = 5$  explants/retina/condition). Ouabain was a potent inducer of glial ripples (Mann–Whitney test,  $p < 0.0001$ ,  $N = 5$  explants for each of five retinas per condition, control ouabain vs aCSF). **C**, Throughout retinal layers, the size of glial ripples in KO retinas was significantly smaller than those in control retinas (Mann–Whitney test,  $p < 0.0001$ ,  $N = 16$  explants for 6 control retinas and 11 explants for 5 KO retinas). Glutamatergic blockers significantly altered the surface area covered by glial ripples in both control and KO retinas (Kruskal–Wallis with multiple comparisons against aCSF: for CNQX,  $p = 0.0028$ ; for AP4,  $p = 0.0595$ ; for AP5,  $p = 0.0216$ ; for TBOA,  $p > 0.9999$ ;  $N = 5$  explants for each of five mice per condition). **D**, **E**, Example fluorescent traces throughout the layers for ROIs displayed in **A** for a representative KO (**E**) and a control (**D**) explant treated with ouabain. non-significant (ns)  $p > 0.05$ , \*  $p \leq 0.05$ , \*\*  $p \leq 0.01$ , \*\*\*\*  $p \leq 0.0001$ .

retinas from distinct animals (Fig. 2H). In the control retina, the profile has peaks at 20–40 and 60–80  $\mu\text{m}$ , possibly corresponding to coordinated activations of the plexiform layers as the descending objective initiated a laser-induced contrast response during acquisition. Comparatively, the KO retinas had an aberrant distribution, with no isolated peaks, and an overall diminished fluorescence compared with control retinas.

During the same recordings of the adult retina in which we analyzed for neural signals (Fig. 3), we observed that clusters of MCs displayed sporadic bursts of spontaneous fluorescence (Fig. 5A,B, Movie 5). These events were identifiable as MC signals because they (1) occurred between neuronal cell bodies, (2) were

visible at different depths of the retina (Fig. 1H) in a synchronized fashion, and (3) displayed slow and broad temporal dynamics (Fig. 5C,E) characteristic of glial signals (Rosa et al., 2015). The spontaneous calcium transients displayed by neurons were much shorter ( $< 4$  s; Fig. 3F) than those of glial cells (5–40 s). Additionally, this pattern of activity corresponded to the expression pattern of GS (Fig. 2C,D), which is found only in MCs in the retina (Bringmann et al., 2009). Of interest, activity was propagated radially to adjacent MCs, in a stereotypical “Ripple” display (Fig. 5B, Movie 6; P20 KO displays a particularly sustained example) sometimes propagating over distances of several hundred micrometers. Figure 5C shows the frequency of these



**Movie 9.** FastZ projections of retinal activity in P61 control GCaMP6f following application of ouabain. [View online]

events as traces in a 10 min recording. At P10, the signal is very active because of the developmental waves present at this age. The traces presented here are normalized to the maximum fluorescence intensity. The fluorescence intensity of these glial ripples is several orders of magnitude above baseline fluorescence, leading to a high signal-to-noise ratio. These glial ripples were rarely seen at P10. In the 20 explants ( $n = 6$  control mice;  $n = 6$  KO mice; multiple explants used per animals; see Materials and Methods) investigated at this age, only three such glial ripples were observed (one control, two KO). By comparison, every 11 min recording from control explants at older ages contains three to five ripples, and those from every KO explant presented more than five ripples (Fig. 5D).

Glial ripples were much rarer than the neuronal waves and wavelets characterized in Figure 3 and appeared at different locations. Indeed, ripples almost never occurred in the same location, activating distinct sets of cells each time. As such, we could not rely on an automatic and pseudorandom detection method, so ripples were identified manually (by an observer blinded to genotype and age), and up to five ripples per explant were used to calculate average distance, duration, and velocity. WT explants displayed frequencies of 0.12 (P15), 0.14 (P20), and 0.16 (P60) ripples per minute, which did not vary with age (Fig. 5D). At each, the ripple frequency observed in KO explants [0.32 (P15), 1.15 (P20), and 0.48 (P60) ripples per minute] was significantly higher than that in controls, with the highest rate seen at P20 (Fig. 5D). Other measures of glial ripples (duration, velocity, and distance) were more variable and did not always reach statistical significance (Fig. 5D–G). KO ripples tended to propagate over further distances than age-matched controls (Fig. 5E) and also tended to last for longer durations (Fig. 5F).

#### Aberrant neuroglial dynamics are driven by dysfunctional glutamatergic signaling

We next sought to characterize the functional and chemical origin of the aberrant neuronal wavelets observed in KO retinas. To locate their origin, we performed four-dimensional simultaneous (FastZ; compare with Materials and Methods) imaging of all retinal layers. We used a simple full-field light stimulus (5 pulses, 1 s ON, 4 s OFF) to identify the ON and OFF portions of the IPL. Although this technique does not enable us to map the dendritic arborizations of individual RGCs, it did identify positive and negative deflections in the fluorescence signal in the labyrinth of processes that make up the IPL. We found that during FastZ

acquisition (six fields imaged simultaneously at 20  $\mu\text{m}$  intervals), we could differentiate the ON and OFF IPLs from their fluorescence deflections in response to light stimulation. Spontaneous (non-light-driven or drug-driven) recordings 9 min long allowed us to image the activity in six different layers at an effective sampling frequency of 1.975 fps. Representative examples of such recordings for both KO and control P60 retinas under standard (vehicle) perfusion conditions are shown in the left portions of Figure 6, A and B. In control explants taken at P60, very little wavelet activity was detected in the INL, IPL, or GCL (Fig. 6A, Movies 7, 8). Consistent with prior results, KO wavelet activity was elevated, especially throughout the IPL and GCL, with less difference seen in the INL (Fig. 6B,C).

Glutamate is the main excitatory neurotransmitter in the retina, with very clear anatomic and functional distinctions in receptor subtypes. We studied the P60 retina using well defined pharmacological agents to block each of the predominant glutamate receptor subtypes. CNQX is a competitive AMPA/kainate receptor antagonist capable of blocking all ionotropic glutamate receptors, including those on OFF bipolar cells (Diamond and Copenhagen, 1993), which are responsible for the propagation of OFF responses from the OPL to the OFF portion of the IPL. L-AP4 is a selective agonist for group III metabotropic glutamate receptors and is used in the retina for blocking mGluR6 receptors on ON-bipolar cells, which are responsible for the propagation of ON responses from the OPL to the ON portion of the IPL (Nakajima et al., 1993). D-AP5 is a selective antagonist for NMDA glutamate receptors, expressed in the inner retina, on RGCs and ACs (Kalloniatis et al., 2004). Only CNQX significantly eradicated the aberrant wavelets (Fig. 6D). The frequency of recorded neural wavelets in the OFF portion of the IPL was significantly smaller in the presence of 10  $\mu\text{M}$  CNQX (Mann–Whitney test,  $p = 0.0043$ ;  $N = 5$  animals). Whereas AP5 (50  $\mu\text{M}$ ) and AP4 (25  $\mu\text{M}$ ) had potentiating effects on the frequencies of recorded waves, the changes were more variable and did not statistically differ ( $p = 0.5556$  for L-AP4;  $p = 0.8571$  for D-AP5;  $N = 8$  animals; Mann–Whitney test). We also used TBOA, to block excitatory amino acid transporters (Derouiche and Rauen, 1995), which are responsible for the first step in the recycling cascade of glutamate. While TBOA induced wavelet-like events, these were present in all retinal layers, thus greatly exceeding the pattern seen in the KO retina.

Unlike neuronal wavelets, glial ripples propagated radially throughout all layers of the retina (Fig. 7A) with the peak fluorescence intensity for each layer phase locked (Fig. 7D). This transretinal coordination is consistent with an MC origin of these signals. Throughout the retina, the frequency of glial ripples in KO retinas was significantly higher than that in control retinas under standard (vehicle) perfusion with aCSF (Fig. 7B). The addition of the glutamate receptor blockers CNQX, AP5, and AP4 to the perfusion did not alter the frequency of glial ripples in either control or KO retinas. In control retinas, the perfusion of GLAST (L-glutamate/L-aspartate transporter) blocker TBOA did not alter the frequency of ripples throughout the retinal layers. Surprisingly, glutamatergic blockers significantly altered the surface area covered by glial ripples in both control and KO retinas, with mixed effects depending on the blocked glutamate receptor. This was also the case for TBOA, confirming a link between glutamatergic signaling and the kinetics of glial ripples (Fig. 7C).

We were able to induce high-frequency ripples throughout retinal layers in the control retina by applying ouabain, an antagonist for the  $\text{Na}^+/\text{K}^+$  ATPase. Increased intracellular sodium



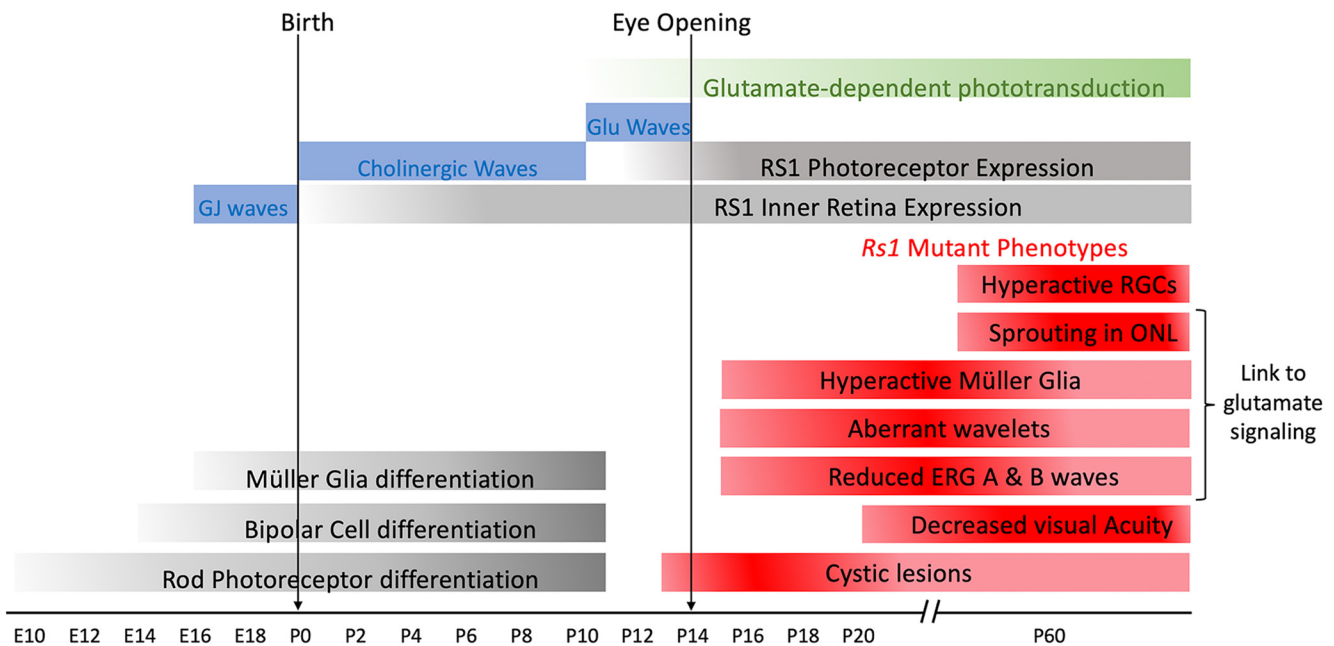


**Figure 8.** Lack of RS1 protein drives excess glutamate and aberrant wavelets. Coincidence of mutant *Rs1* phenotypes with maturation of glutamatergic synapses. Some of the phenotypes observed in models of XLRS have been linked to glutamatergic signaling.

reduces the activity of the sodium–calcium exchanger, which pumps one calcium ion out of the cell and three sodium ions into the cell down their concentration gradient. This leads to an increase in intracellular calcium, and the eventual death of the cell/tissue, in a very repeatable and sequential manner, ending with high-frequency glial ripples (Fig. 7*B,D,E*, Movie 9).

## Discussion

### Schisis, neuronal wavelets, glial ripples, glutamate dependency

As a follow-up to our observation that *Rs1* expression is initiated between P7 and P14 (Liu et al., 2019), we sought to identify markers of dysfunction associated with the lack of the RS1 protein in the early postnatal retina. We confirmed *Rs1* RNA expression and detectable RS1 protein in photoreceptor inner segments at P5 and P9, respectively. We further identified both structural and physiological phenotypes in *Rs1* mutant mice from postnatal day 13, revealing a 4 d lag in the role for the protein in the control of retinal structure and function. These phenotypes presented in the forms of cystic lesions observable by OCT *in vivo* and the appearance of aberrant wavelets of neural activity. Indeed, all three *Rs1* mutant mouse models (KO, C59S, R141C) displayed a similar temporal appearance of schisis, which provides evidence that the mouse strains used in the study are valid models of human disease (Molday et al., 2012). Our investigations of the mechanisms underlying the novel phenotype of aberrant wavelets in the KO also revealed a link to glutamate signaling, a key neurotransmitter in retinal development and function.

### Calcium imaging for dissecting retinal function and dysfunction

Most functional studies of *Rs1* mutant mouse lines have focused on whole animal measures (OCT imaging, electroretinography) that provide links to key phenotypic features of XLRS patients (Weber et al., 2002; Zeng et al., 2004; Jablonski et al., 2005; Chen et al., 2017). In our previous work (Liu et al., 2019), we noted

severe disease phenotypes in mice aged P15 in an allelic series of three *Rs1* mutants. In these animals, spontaneous aberrant activity in RGCs was revealed using patch-clamp electrophysiology. Whereas this approach provided evidence of altered synaptic organization of individual neurons, the technique is limited to the examination healthy cells that can be patched successfully, as it is near impossible to establish and maintain a giga-ohm seal with an intracellular pipette on dystrophic cell membranes. Patch-clamp electrophysiology is thus not optimal to evaluate the dynamics of unhealthy retinal neurons. Multiphoton microscopy of mouse lines expressing the fluorescent calcium sensor GCaMP6f avoids this shortfall and has the additional feature of allowing intracellular calcium dynamics to be acquired simultaneously from cells in all retinal layers.

The dataset we have generated in the present study has enabled us to investigate the intricacies of physiological activity upstream of these hyperactive RGCs, and concurrently in neuroglial cell populations. Imaging of intracellular calcium dynamics has been essential for exposing and dissecting spontaneous developmental waves (Meister et al., 1991). The advent of multiphoton imaging has also expanded our ability to characterize RGC and bipolar cell function (Baden et al., 2016; Franke et al., 2017; Baden et al., 2020). In addition, the increased availability of selective promoters and transgenic mouse lines has enabled the targeting of distinct cell populations. Recent examples include the imaging of retinal MCs during development (Rosa et al., 2015) and vascular signaling in the retina, leading to a 3D mapping of the pericyte connectome (Alarcon-Martinez et al., 2020; Kovacs-Oller et al., 2020). In an effort to take advantage of these tools, we developed a new *Rs1*-deficient mouse line with ubiquitous expression of a fast intracellular calcium signaling sensor, and with it, we documented the coordinated activation of connected columns of MCs in both the healthy control and KO retinas (glial ripples). The further characterization of these events and their underlying physiological mechanisms in these and other models should help to elucidate the cellular substrates underlying functional hyperemia by the neural–glial–vascular unit.

### Role of RS1 in development

It is well established that *Rs1* is almost exclusively expressed by photoreceptors, but that the RS1 protein is present throughout the retina (Takada et al., 2004). In this study, we examined the developmental time course over which these features emerge, with the goal of clarifying the cellular events that accompany the earliest functional and structural defects. Our dataset supports the premise that RS1 serves as more than just an extracellular adhesion protein maintaining retinal integrity. Previous studies identified the  $\beta 2$  subunit of the retina-specific Na/K-ATPase as an interacting partner for retinoschisin (Molday et al., 2007), which is essential for anchoring Na/K-ATPase to the plasma membrane (Friedrich et al., 2011) of photoreceptors. More recent work has also demonstrated that RS1 acts as an antiapoptotic regulator of mitogen-activated protein kinase signaling in the retina (Plössl et al., 2017a), via its interactions with Na/K-ATPase (Plössl et al., 2017b). Our data bring a multicellular and developmental context to these molecular findings. Specifically, that RS1 plays a key role in regulating the highly coordinated appearance of distinct anatomic and physiological phenotypes of glutamatergic synapses at the IPL and OPL during development (Fig. 8). Furthermore, they identify an early window of time in development in which RS1 could have additional protein interactions.

Normally in mice, P11 marks the end of rod, BC, and MC differentiation (Young, 1985), and the onset of the maturation stage for the photoreceptor-to-BC synapses (Stage III waves), which exposes the retina to glutamate (Bansal et al., 2000) and primes the visual system for visual experience at eye opening (P15). Our data suggest that this process is disrupted in the absence of RS1, building on previous work that highlighted anatomic (Liu et al., 2019) and physiological (Ou et al., 2015) disruptions at the OPL. For example, Ou et al. (2015) found presynaptic and postsynaptic defects at the photoreceptor-to-BC synapse in mice models of XLRS. Our recent study also revealed ectopic neurites from BCs and HCs (Liu et al., 2019). Thus, the lack of such a multifaceted protein in development may lead to maladaptive cellular changes that have the potential to impact visual processing into adult life, which would need to be considered when developing treatments for XLRS patients.

### Implications for development and repair strategies

Disruption of the spontaneous waves that guide normal visual development leads to a disruption of RGC projections to central targets. Retinal wave activity is essential for the normal wiring of RGC receptive fields, begetting the maturation of their (Stage I) electrical synapses, (Stage II) cholinergic synapses, and (Stage III) glutamatergic synapses (Feller et al., 1996; Feller, 2009; Maccione et al., 2014). Our finding that glutamatergic transmission is disrupted in parallel with the presence of stage III waves, indicates that there is potential for the desegregation of inputs to central targets, and the enduring abnormal connectivity.

Indeed, treatment strategies for XLRS have had limited therapeutic efficacy. Evidence that the outer retinal structure and function of *Rs1* KO mice could be improved by gene replacement therapy (Molday et al., 2006; Takada et al., 2008; Dalkara et al., 2013; Ou et al., 2015) was used to justify a retinal AAV8-RS1 gene therapy phase I/IIa clinical trial (Cukras et al., 2018) in adult subjects. However, the trial failed to replicate the observations made in mouse models and also revealed evidence that the vector induced deleterious inflammation (Mishra et al., 2021). With an age range of 23–72 years across nine participants, the results of this clinical trial may instead highlight the need for RS1

in development to generate fully functional visual systems. Similar trials performed in much younger patients before abnormal retinal structure and function are entrenched may have potential for a better outcome, but such studies would be dependent on an improved understanding of time course and location of RS1 expression in the human retina. Such information might be obtained from the study of retinal organoids derived from induced pluripotent stem cells (Hallam et al., 2018).

It is crucial that future studies determine whether retinoschisis leads to the formation of aberrant retinothalamic circuits, as studies have done for other models of retinal disease (Demas et al., 2006). In humans, such information may also be derived from studies of central visual pathways using noninvasive techniques such as EEG, tensor diffusion imaging, and psychophysical tests designed to test the ability to process noisy images (McAnany et al., 2022).

### Implications for repair strategies in adult patients

Repeated attempts to treat XLRS with carbonic anhydrase inhibitors to reduce cystic volume have not led to sustainable clinical improvements in visual perception (Thobani and Fishman, 2011; Pennesi et al., 2018; Testa et al., 2019; Ambrosio et al., 2021), which suggests that XLRS patients have functional symptoms of disease that are independent of the structural phenotype. Indeed, our study provides a set of biomarkers for such functional abnormalities. This information should stimulate drug discovery efforts directed toward the reversal of wavelets or glial ripples that would not affect retinal processing in the mature *GCaMP<sup>+/−</sup>; Rs1<sup>−/−</sup>* retina.

### References

- Alam NM, Douglas RM, Prusky GT (2022) Treatment of age-related visual impairment with a peptide acting on mitochondria. *Dis Model Mech* 15: dmm048256.
- Alarcon-Martinez L, Villafranca-Baughman D, Quintero H, Kacerovsky JB, Dotigny F, Murai KK, Prat A, Drapeau P, Di Polo A (2020) Interpericyte tunnelling nanotubes regulate neurovascular coupling. *Nature* 585:91–95.
- Alexander KR, Barnes CS, Fishman GA (2005) Characteristics of contrast processing deficits in X-linked retinoschisis. *Vision Res* 45:2095–2107.
- Allen AE, Storch R, Martial FP, Petersen RS, Montemurro MA, Brown TM, Lucas RJ (2014) Melanopsin-driven light adaptation in mouse vision. *Curr Biol* 24:2481–2490.
- Ambrosio L, Williams JS, Gutierrez A, Swanson EA, Munro RJ, Ferguson RD, Fulton AB, Akula JD (2021) Carbonic anhydrase inhibition in X-linked retinoschisis: an eye on the photoreceptors. *Exp Eye Res* 202:108344.
- Baden T, Berens P, Franke K, Román Rosón M, Bethge M, Euler T (2016) The functional diversity of retinal ganglion cells in the mouse. *Nature* 529:345–350.
- Baden T, Euler T, Berens P (2020) Understanding the retinal basis of vision across species. *Nat Rev Neurosci* 21:5–20.
- Bansal A, Singer JH, Hwang BJ, Xu W, Beaudet A, Feller MB (2000) Mice lacking specific nicotinic acetylcholine receptor subunits exhibit dramatically altered spontaneous activity patterns and reveal a limited role for retinal waves in forming ON and OFF circuits in the inner retina. *J Neurosci* 20:7672–7681.
- Bell BA, Kaul C, Hollyfield JG (2014) A protective eye shield for prevention of media opacities during small animal ocular imaging. *Exp Eye Res* 127:280–287.
- Bell BA, Kaul C, Bonilha VL, Rayborn ME, Shadrach K, Hollyfield JG (2015) The BALB/c mouse: effect of standard vivarium lighting on retinal pathology during aging. *Exp Eye Res* 135:192–205.
- Bringmann A, Pannicke T, Biedermann B, Francke M, Iandiev I, Grosche J, Wiedemann P, Albrecht J, Reichenbach A (2009) Role of retinal glial cells in neurotransmitter uptake and metabolism. *Neurochem Int* 54:143–160.



- Bush M, Setiawati D, Yip CK, Molday RS (2016) Cog-wheel octameric structure of RS1, the discoidin domain containing retinal protein associated with X-linked retinoschisis. *PLoS One* 11:e0147653.
- Chen D, Xu T, Tu M, Xu J, Zhou C, Cheng L, Yang R, Yang T, Zheng W, He X, Deng R, Ge X, Li J, Song Z, Zhao J, Gu F (2017) Recapitulating X-linked juvenile retinoschisis in mouse model by knock-in patient-specific novel mutation. *Front Mol Neurosci* 10:453.
- Chen T-W, Wardill TJ, Sun Y, Pulver SR, Renninger SL, Baohan A, Schreier ER, Kerr RA, Orger MB, Jayaraman V, Looger LL, Svoboda K, Kim DS (2013) Ultrasensitive fluorescent proteins for imaging neuronal activity. *Nature* 499:295–300.
- Cukras C, Wiley HE, Jeffrey BG, Sen HN, Turriff A, Zeng Y, Vijayarathay C, Marangoni D, Ziccardi L, Kjellstrom S, Park TK, Hiriyanna S, Wright JF, Colosi P, Wu Z, Bush RA, Wei LL, Sieving PA (2018) Retinal AAV8-RS1 gene therapy for X-linked retinoschisis: initial findings from a phase I/IIa trial by intravitreal delivery. *Mol Ther* 26:2282–2294.
- Dalkara D, Byrne LC, Klimczak RR, Visel M, Yin L, Merigan WH, Flannery JG, Schaffer DV (2013) In vivo-directed evolution of a new adeno-associated virus for therapeutic outer retinal gene delivery from the vitreous. *Sci Transl Med* 5:189ra176.
- Demas J, Sagdullaev BT, Green E, Jaubert-Miazza L, McCall MA, Gregg RG, Wong ROL, Guido W (2006) Failure to maintain eye-specific segregation in nob, a mutant with abnormally patterned retinal activity. *Neuron* 50:247–259.
- Derouiche A, Rauen T (1995) Coincidence of L-glutamate/L-aspartate transporter (GLAST) and glutamine synthetase (GS) immunoreactions in retinal glia: evidence for coupling of GLAST and GS in transmitter clearance. *J Neurosci Res* 42:131–143.
- Diamond JS, Copenhagen DR (1993) The contribution of NMDA and non-NMDA receptors to the light-evoked input-output characteristics of retinal ganglion cells. *Neuron* 11:725–738.
- Feller MB (2009) Retinal waves are likely to instruct the formation of eye-specific retinogeniculate projections. *Neural Dev* 4:24.
- Feller MB, Wellis DP, Stellwagen D, Werblin FS, Shatz CJ (1996) Requirement for cholinergic synaptic transmission in the propagation of spontaneous retinal waves. *Science* 272:1182–1187.
- Forsius H, Krause U, Helve J, Vuopala V, Mustonen E, Vainio-Mattila B, Fellman J, Eriksson AW (1973) Visual acuity in 183 cases of X-chromosomal retinoschisis. *Can J Ophthalmol* 8:385–393.
- Franke K, Berens P, Schubert T, Bethge M, Euler T, Baden T (2017) Inhibition decorrelates visual feature representations in the inner retina. *Nature* 542:439–444.
- Friedrich U, Stöhr H, Hilfinger D, Loenhardt T, Schachner M, Langmann T, Weber BH (2011) The Na/K-ATPase is obligatory for membrane anchorage of retinoschisin, the protein involved in the pathogenesis of X-linked juvenile retinoschisis. *Hum Mol Genet* 20:1132–1142.
- Gargini C, Terzibasi E, Mazzoni F, Strettoi E (2007) Retinal organization in the retinal degeneration 10 (rd10) mutant mouse: a morphological and ERG study. *J Comp Neurol* 500:222–238.
- George ND, Yates JR, Moore AT (1995) X linked retinoschisis. *Br J Ophthalmol* 79:697–702.
- Govardovskii VI, Calvert PD, Arshavsky VY (2000) Photoreceptor light adaptation. Untangling desensitization and sensitization. *J Gen Physiol* 116:791–794.
- Hallam D, Hilgen G, Dorgau B, Zhu L, Yu M, Bojic S, Hewitt P, Schmitt M, Uteng M, Kustermann S, Steel D, Nicholds M, Thomas R, Treumann A, Porter A, Sernagor E, Armstrong L, Lako M (2018) Human-induced pluripotent stem cells generate light responsive retinal organoids with variable and nutrient-dependent efficiency. *Stem Cells* 36:1535–1551.
- Hippert C, Graca AB, Barber AC, West EL, Smith AJ, Ali RR, Pearson RA (2015) Müller glia activation in response to inherited retinal degeneration is highly varied and disease-specific. *PLoS One* 10:e0120415.
- Ivanova E, Toychiev AH, Yee CW, Sagdullaev BT (2013) Optimized protocol for retinal wholemount preparation for imaging and immunohistochemistry. *J Vis Exp*. doi: 10.3791/51018.
- Jablonski MM, Dalke C, Wang XFei, Lu L, Manly KF, Pretsch W, Favor J, Pardue MT, Rinchik EM, Williams RW, Goldowitz D, Graw J (2005) An ENU-induced mutation in Rslh causes disruption of retinal structure and function. *Mol Vis* 11:569–581.
- Jones BW, Watt CB, Marc RE (2005) Retinal remodeling. *Clin Exp Optom* 88:282–291.
- Jones BW, Kondo M, Terasaki H, Lin Y, McCall M, Marc RE (2012) Retinal remodeling. *Jpn J Ophthalmol* 56:289–306.
- Kalloniatis M, Sun D, Foster L, Haverkamp S, Wässle H (2004) Localization of NMDA receptor subunits and mapping NMDA drive within the mammalian retina. *Vis Neurosci* 21:587–597.
- Kovacs-Oller T, Ivanova E, Bianchimano P, Sagdullaev BT (2020) The pericyte connectome: spatial precision of neurovascular coupling is driven by selective connectivity maps of pericytes and endothelial cells and is disrupted in diabetes. *Cell Discov* 6:39.
- Liu Y, Kinoshita J, Ivanova E, Sun D, Li H, Liao T, Cao J, Bell BA, Wang JM, Tang Y, Brydges S, Peachey NS, Sagdullaev BT, Romano C (2019) Mouse models of X-linked juvenile retinoschisis have an early onset phenotype, the severity of which varies with genotype. *Hum Mol Genet* 28:3072–3090.
- Maccione A, Hennig MH, Gandolfo M, Muthmann O, van Coppenhagen J, Eglen SJ, Berdondini L, Sernagor E (2014) Following the ontogeny of retinal waves: pan-retinal recordings of population dynamics in the neonatal mouse. *J Physiol* 592:1545–1563.
- McAnany JJ, Park JC, Fishman GA, Hyde RA (2022) Contrast sensitivity and equivalent intrinsic noise in X-linked retinoschisis. *Transl Vis Sci Technol* 11:7.
- Meister M, Wong RO, Baylor DA, Shatz CJ (1991) Synchronous bursts of action potentials in ganglion cells of the developing mammalian retina. *Science* 252:939–943.
- Mishra A, Vijayarathay C, Cukras CA, Wiley HE, Sen HN, Zeng Y, Wei LL, Sieving PA (2021) Immune function in X-linked retinoschisis subjects in an AAV8-RS1 phase I/IIa gene therapy trial. *Mol Ther* 29:2030–2040.
- Molday LL, Min S-H, Seeliger MW, Wu WWH, Dinculescu A, Timmers AM, Janssen A, Tonagel F, Hudl K, Weber BHF, Hauswirth WW, Molday RS (2006) Disease mechanisms and gene therapy in a mouse model for X-linked retinoschisis. *Adv Exp Med Biol* 572:283–289.
- Molday LL, Wu WW, Molday RS (2007) Retinoschisin (RS1), the protein encoded by the X-linked retinoschisis gene, is anchored to the surface of retinal photoreceptor and bipolar cells through its interactions with a Na/K ATPase-SARM1 complex. *J Biol Chem* 282:32792–32801.
- Molday RS, Kellner U, Weber BH (2012) X-linked juvenile retinoschisis: clinical diagnosis, genetic analysis, and molecular mechanisms. *Prog Retin Eye Res* 31:195–212.
- Nakajima Y, Iwakabe H, Akazawa C, Nawa H, Shigemoto R, Mizuno N, Nakanishi S (1993) Molecular characterization of a novel retinal metabotropic glutamate receptor mGluR6 with a high agonist selectivity for L-2-amino-4-phosphonobutyrate. *J Biol Chem* 268:11868–11873.
- Ou J, Vijayarathay C, Ziccardi L, Chen S, Zeng Y, Marangoni D, Pope JG, Bush RA, Wu Z, Li W, Sieving PA (2015) Synaptic pathology and therapeutic repair in adult retinoschisis mouse by AAV-RS1 transfer. *J Clin Invest* 125:2891–2903.
- Peachey NS, Fishman GA, Derlacki DJ, Brigell MG (1987) Psychophysical and electroretinographic findings in X-linked juvenile retinoschisis. *Arch Ophthalmol* 105:513–516.
- Pennesi ME, Birch DG, Jayasundera KT, Parker M, Tan O, Gurses-Ozden R, Reichley C, Beasley KN, Yang P, Weleber RG, Bennett LD, Heckenlively JR, Kothapalli K, Chulay JD (2018) Prospective evaluation of patients with X-linked retinoschisis during 18 months. *Invest Ophthalmol Vis Sci* 59:5941–5956.
- Plössl K, Weber BH, Friedrich U (2017a) The X-linked juvenile retinoschisis protein retinoschisin is a novel regulator of mitogen-activated protein kinase signalling and apoptosis in the retina. *J Cell Mol Med* 21:768–780.
- Plössl K, Royer M, Bernklau S, Tavraz NN, Friedrich T, Wild J, Weber BHF, Friedrich U (2017b) Retinoschisin is linked to retinal Na/K-ATPase signaling and localization. *Mol Biol Cell* 28:2178–2189.
- Prusky GT, Alam NM, Beekman S, Douglas RM (2004) Rapid quantification of adult and developing mouse spatial vision using a virtual optomotor system. *Invest Ophthalmol Vis Sci* 45:4611–4616.
- Rosa JM, Bos R, Sack GS, Fortuny C, Agarwal A, Bergles DE, Flannery JG, Feller MB (2015) Neuron-glia signaling in developing retina mediated by neurotransmitter spillover. *Elife* 4:e09590.
- Sauer CG, Gehrig A, Warneke-Wittstock R, Marquardt A, Ewing CC, Gibson A, Lorenz B, Jurklies B, Weber BH (1997) Positional cloning of the gene associated with X-linked juvenile retinoschisis. *Nat Genet* 17:164–170.
- Takada Y, Fariss RN, Tanikawa A, Zeng Y, Carper D, Bush R, Sieving PA (2004) A retinal neuronal developmental wave of retinoschisin expression

- begins in ganglion cells during layer formation. *Invest Ophthalmol Vis Sci* 45:3302–3312.
- Takada Y, Vijayasarathy C, Zeng Y, Kjellstrom S, Bush RA, Sieving PA (2008) Synaptic pathology in retinoschisin knockout (Rs1<sup>-/-</sup>) mouse retina and modification by rAAV-Rs1 gene delivery. *Invest Ophthalmol Vis Sci* 49:3677–3686.
- Tanino T, Katsumi O, Hirose T (1985) Electrophysiological similarities between two eyes with X-linked recessive retinoschisis. *Doc Ophthalmol* 60:149–161.
- Testa F, Di Iorio V, Gallo B, Marchese M, Nesti A, De Rosa G, Melillo P, Simonelli F (2019) Carbonic anhydrase inhibitors in patients with X-linked retinoschisis: effects on macular morphology and function. *Ophthalmic Genet* 40:207–212.
- Thobani A, Fishman GA (2011) The use of carbonic anhydrase inhibitors in the retreatment of cystic macular lesions in retinitis pigmentosa and X-linked retinoschisis. *Retina* 31:312–315.
- Tolun G, Vijayasarathy C, Huang R, Zeng Y, Li Y, Steven AC, Sieving PA, Heymann JB (2016) Paired octamer rings of retinoschisin suggest a junctional model for cell-cell adhesion in the retina. *Proc Natl Acad Sci U S A* 113:5287–5292.
- Weber BHF, Schrewe H, Molday LL, Gehrig A, White KL, Seeliger MW, Jaissle GB, Friedburg C, Tamm E, Molday RS (2002) Inactivation of the murine X-linked juvenile retinoschisis gene, Rs1h, suggests a role of retinoschisin in retinal cell layer organization and synaptic structure. *Proc Natl Acad Sci U S A* 99:6222–6227.
- Wu WW, Wong JP, Kast J, Molday RS (2005) RS1, a discoidin domain-containing retinal cell adhesion protein associated with X-linked retinoschisis, exists as a novel disulfide-linked octamer. *J Biol Chem* 280:10721–10730.
- Young RW (1985) Cell differentiation in the retina of the mouse. *Anat Rec* 212:199–205.
- Yu DY, Cringle S, Valter K, Walsh N, Lee D, Stone J (2004) Photoreceptor death, trophic factor expression, retinal oxygen status, and photoreceptor function in the P23H rat. *Invest Ophthalmol Vis Sci* 45:2013–2019.
- Zeng Y, Takada Y, Kjellstrom S, Hiriyanna K, Tanikawa A, Wawrousek E, Smaoui N, Caruso R, Bush RA, Sieving PA (2004) RS-1 gene delivery to an adult Rs1h knockout mouse model restores ERG b-wave with reversal of the electronegative waveform of X-linked retinoschisis. *Invest Ophthalmol Vis Sci* 45:3279–3285.
- Zhu X, Bergles DE, Nishiyama A (2008) NG2 cells generate both oligodendrocytes and gray matter astrocytes. *Development* 135:145–157.